Sapienza Università di Roma

Dipartimento di Ingegneria Astronautica, Elettrica ed Energetica

Dottorato di Ricerca Energia ed Ambiente – XXX CICLO

Investigation on Space Navigation Techniques based on Optical Sensors

Advisor:

Prof. Giovanni B. Palmerini

PhD Candidate:

Emanuele Medaglia

A. A. 2016/2017

Introduction to the thesis

Space navigation deals with the determination of the kinematic state (position, velocity, attitude) of a spacecraft. The kinematic state can be obtained based on the output of suitable sensors and by means of appropriate computation. As far as it concerns the sensors, the optoelectronic ones – already present – are facing increasing interest and applications. The success of these sensors depends on the improved performance, the reduced cost (also as a result of a strong commercial growth for parent terrestrial products) as well as on the availability of computation resources required to efficiently process the images. It clearly appears that the interest for these sensing technologies will continue in the future, and their application will spread to all classes of space platforms, including the small cubesats.

The thesis is devoted to investigate some aspects related to the use of the optoelectronic sensors – indeed the word *techniques* – on-board spacecraft.

First, the focus is on the star tracker, deemed as the most accurate (and the most expensive) of the attitude sensors, and considered to be the flagship of the space optoelectronic instrument, with complex hardware and strong computational requirements. The two initial chapters are devoted to resume star tracker basics and to recall the attitude determination techniques.

Then, the following part of the thesis deals with some more original contribution considering the calibration of the star trackers. This is a topic of high current interest as it greatly affects the cost of the hardware. Instead of carrying on long expensive test campaign at the facility, a simpler and faster two steps process with a "raw", preparatory phase at the production site and a final, possibly autonomous, accurate calibration once in orbit can produce valuable results. The third chapter reports the simulations and the findings for this proposed technique.

Some more general discussion is required to introduce the last part of this dissertation. Space probes increasingly explore the solar system, up to faraway planets. Orbit determination of these probes, based on radio tracking from Earth, becomes clearly less accurate as the distance from Earth increases. Above all, the time required for telemetry/navigation data downlink and tele-command uplink also increases with distance from Earth and therefore real-time manoeuvres and operations become impossible. When a spacecraft is close to a planetary target (or celestial body, including comets and asteroids), optical navigation

– in use since the experiments with Mariner 6 and 7 missions to Mars (1969) – can nowadays ensures accurate estimates of the relative kinematics and allows to conceive manoeuvres computed on-board, autonomously and in real time. This technique, based on imaging and on the comparison with already known data as previously captured images, celestial catalogues or ephemerides, helps with the determination of the complete kinematic state of the spacecraft, relative to the target. Indeed, it is similar to attitude determination traditionally carried out by means of star trackers, where the spacecraft's orientation is computed thanks to a priori information included in the star catalogue. The similarity in concept, with imaging process and comparison to stored information, introduces the question if star tracker's and proximity cameras' functions can be exploited by the same on-board hardware. The availability of a universal optical navigation sensor, sharing a large part of its expensive components, could really be an enabling technology for a more effective space exploration.

The aim of this study is to investigate and analyse this possibility, which is collecting more and more interest. The main issue is the identification of the sensor's configuration – as an example beginning with multi-head star trackers with different optics and focal lengths – and algorithms allowing to improving star trackers performances and to exploit this twin use. This identification

moves through a correct modelling of the sensor behaviour. The combination between star trackers and proximity cameras as position/attitude sensors could obviously allow a reduction in costs, and – probably more important at the current, preliminary status of this approach – provide a back-up solution in case of failures thanks a possible, even non-optimal redundancy. Furthermore, the interest of this study is not limited to deep space missions, and may be extended to other vehicles currently using star trackers and cameras as the planetary rovers.

List of contents

Part I

Star Tracker and Attitude Determination

1

Star Tracker

1.1. Overview

Star Trackers are optoelectronic instruments providing the attitude of the satellites through star observations and are considered among the most accurate attitude sensors. The estimate of spacecraft attitude is obtained starting from the measurements of star coordinates in the body reference frame and comparing these "observed" coordinates with the "known" star directions stored in the on-board star catalogue [1].

A CCD detector reveals the observed stars in the field of view (FOV) of the sensor. On the basis of the classical pinhole scheme [1] [2] the data processing section of the Star Tracker is capable to associate a unit vector (or a line of sight) to each captured star (see Fig. 2).

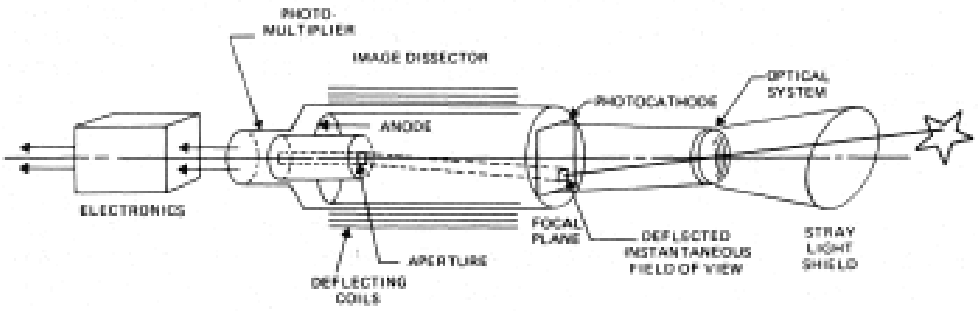

Fig. 1 – Example of Star Tracker HW [1]

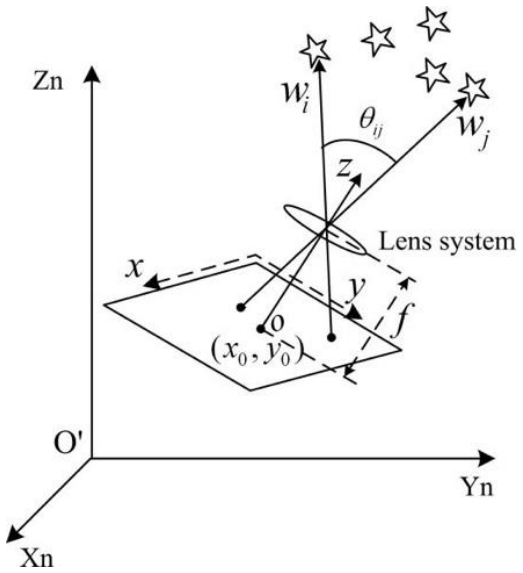

Fig. 2 – Model of Star Tracker: projection of stars on CCD detector [3]

An example of the image captured by the star tracker is represented in Fig. 3, produced with the simulator prepared and used for this research work.

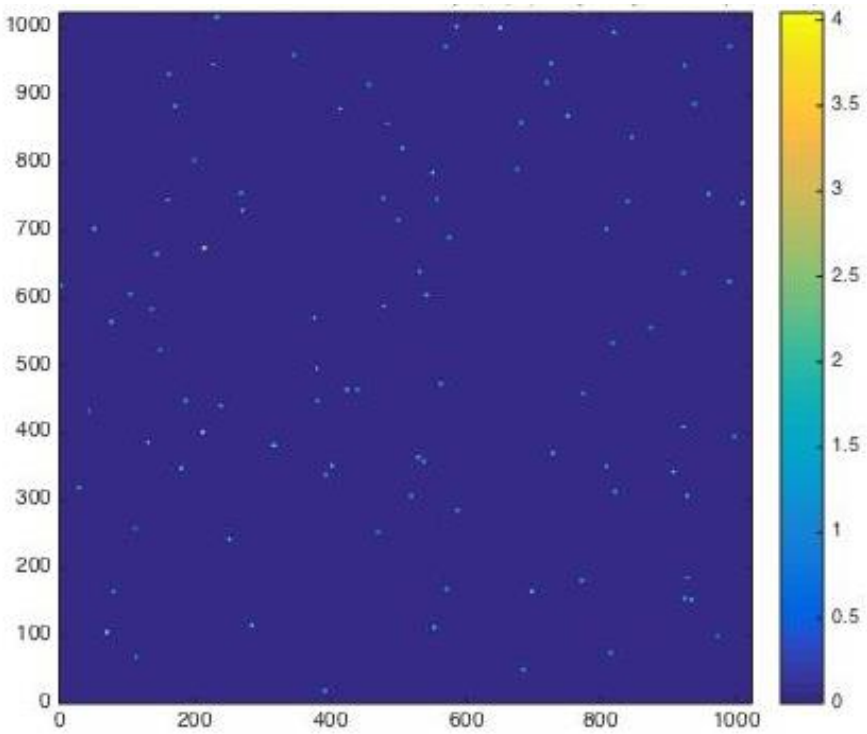

Fig. 3 – Observed stars on Star Tracker detector (CCD)

The Star Tracker can identify the stars in the image with the corresponding ones in a catalogue available on-board based on the measurements of the angles between them in the two frames, i.e. the angles among the measured lines of sight in the Star Tracker reference frame and the ones reported by the catalogue in an inertial reference frame. In fact, the inter-star angles are invariant with respect to the rotation transformation operated on the point of view. Let $\hat{\boldsymbol{v}}_{\boldsymbol{i}}$ and $\hat{\boldsymbol{v}}_{\boldsymbol{j}}$ the *i-th* and *j-th* star catalogued unit vectors

in the inertial reference frame $O' - X_n Y_n Z_n$, $\hat{\boldsymbol{w}}_{\boldsymbol{i}}$ and $\hat{\boldsymbol{w}}_{\boldsymbol{j}}$ the *i-th* and *j-th* measured star vectors in the sensor reference frame $o' - xyz$, (see Fig. 2), then:

$$\hat{\boldsymbol{v}}_{\boldsymbol{i}}^{\boldsymbol{T}} \hat{\boldsymbol{v}}_{\boldsymbol{j}} = \hat{\boldsymbol{w}}_{\boldsymbol{i}}^{\boldsymbol{T}} \hat{\boldsymbol{w}}_{\boldsymbol{j}} \tag{2-1}$$

Once the stars have been identified, the rotation transforming the body-frame observation vectors to the inertial frame catalogue vectors offers the attitude matrix.

This attitude estimate clearly depends on the performance of the overall sensors' chain, in terms of imaging, signal processing, computation algorithm, catalogue accuracy. Considering the imaging part, a significant contribution is given by a precise knowledge of the optical characteristics, as focal length (f), offset of the bore-sight (x_0, y_0) and possible focal plane optical distortions [4] [5]. Indeed, from Fig. 2 the module of measured star unit vectors $\hat{\boldsymbol{w}}$, in the case the sensor is not affected by focal plane optical distortion, is:

$$|\hat{\boldsymbol{w}}| = \frac{1}{\sqrt{(x-x_0)^2+(y-y_0)^2+f^2}} \begin{bmatrix} -(x-x_0) \\ -(y-y_0) \\ f \end{bmatrix} \tag{2-2}$$

1.2. Characteristics

A typical architecture of a star tracker is represented in the following figure [1]:

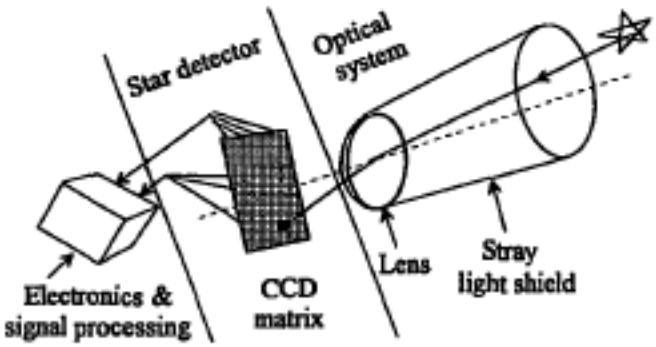

Fig. 4 – Star Tracker HW architecture [1]

The main HW components are:

- **Optical System**, composed by two main elements:
    1. **Lens system**, that converges the stars' light into the focus of the optical head and filters the desired wavelength of the stars' light;

    2. **Stray-light shield**, that protects the detector from undesired light sources (e.g. Sun light, Earth albedo, moonlight, light reflections, …). Without this shield, the Star Sensor can become inoperable.

- **Detectors for Starlight**, that detects the presence of stellar images and their coordinates in matrix board. Nowadays are generally used two types of detectors:
    1. **CCD** (*Charge Coupled Device*), that is a solid-state integrated circuit, built as a matrix of photosensitive semiconductor elements called pixels. The standard CCD size is 512 x 512 pixels, providing a good angular resolution. The CCD detector has a scanning mechanism that records any illuminated cell. The charge collected by the cell is stored in horizontal and vertical sliding registers and transfer to the electrics without any treatment (see Fig. 5).

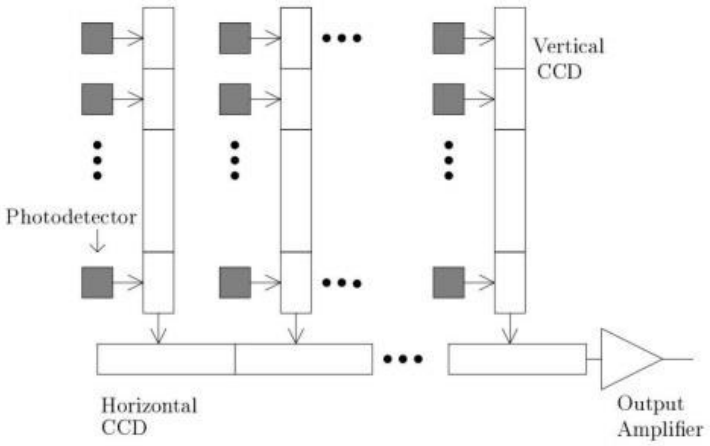

Fig. 5 – CCD detector

There is an amplification of the signal for each read-out channel; in the scheme reported in Fig. 5 there is only one channel. The output of the CCD detector is an analogic signal.

2. **CMOS** (*Complementary Metal-Oxide-Semiconductor*), type **APS** (Active-Pixel Sensor), that is an integrated circuit containing a matrix of pixel sensors, each pixel containing a photo-detector and an active amplifier. The standard APS size is 1024x1024 pixels.

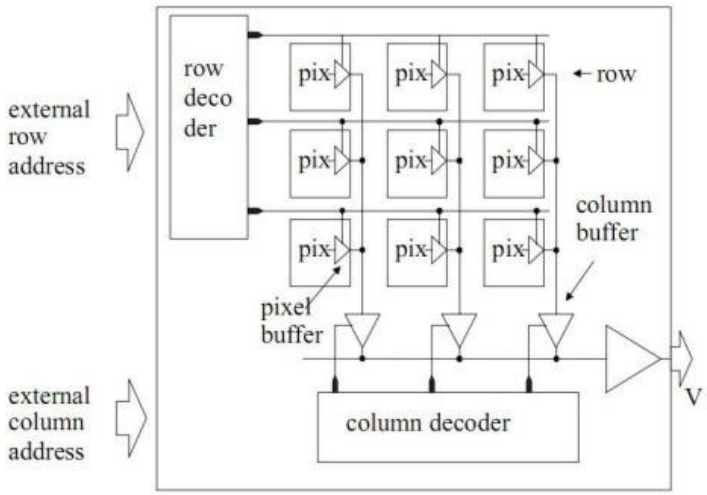

Fig. 6 – APS detector

Differently from the CCD detector, there is an amplification of the signal for each single pixel, for each column and read-out channel (see Fig. 6). The output of the APS detector is a digital signal.

- **Electronics and Signal Processing HW**. The Electronics allows to properly operate to the HW, the CPU and the Memory Units. The Signal Processing HW elaborates the signal coming from the detector, calculates the star coordinates, comparing with the information stored in the on-board catalogue, and provides the estimate of attitude.

2

Attitude determination

2.1. Attitude determination

The problem to determine the orientation, pointing or *attitude* of a spacecraft can be solved in different ways. The simplest one is to specify the relative orientation of a triad with respect to some reference coordinate frame.

2.1.1. Reference frames

In this paragraph are introduced the reference frames that will be used in the following for the attitude determination of the spacecraft. In particular, the basic types of coordinate systems are four:

- Fixed relative to the body of the spacecraft;
- Fixed in inertial space;
- Relative to the orbit and not fixed to either the spacecraft or inertial space.
- Fixed relative to the target

Body reference frame

The body reference frame, defined by orthogonal, right-handed triad $\hat{\mathbf{i}}, \hat{\mathbf{j}}, \hat{\mathbf{k}}$, such as:

$$\hat{\mathbf{i}} \times \hat{\mathbf{j}} = \hat{\mathbf{k}} \tag{3-1}$$

is the reference frame fixed to the spacecraft bus. As the sensors are rigidly mounted to the bus, the measurements coming from the star trackers are taken in this reference frame.

Inertial reference frame

The commonly accepted inertial reference frame is defined as a non-rotating frame, with origin in the centre of Earth and axes X, Y, Z defined with respect to the fixed stars [1] [6]. The X-axis, also

called vernal axis, is oriented towards the Aries point (or vernal point)[1]; the Z-axis is coincident to the Earth rotation axis and oriented towards the North pole; the Y-axis completes a right-hand orthogonal axis frame. The unit vectors triad individuating the Inertial Reference Frame is $\hat{\boldsymbol{c}}_1$, $\hat{\boldsymbol{c}}_2$, $\hat{\boldsymbol{c}}_3$, respectively directed towards X, Y and Z axes. Due to the precession of the equinoxes, an apparent movement of the star (star motion) occurs in this system at the rate of approximately 50 arcsec per year. For this reason, it is necessary to associate a date to this kind of system. The most commonly used systems are 1950 coordinates, 2000 coordinates (J2000) and true of date [1].

Orbit reference frame

The Orbit-Defined reference frame, defined by orthogonal, right-handed triad $\hat{\mathbf{r}}, \hat{\boldsymbol{\vartheta}}, \hat{\mathbf{h}}$, such as:

$$\hat{\mathbf{r}} \times \hat{\boldsymbol{\vartheta}} = \hat{\mathbf{h}} \tag{3-2}$$

The $\hat{\boldsymbol{r}}$ axis is parallel to the orbital radius of the spacecraft, positive outward from the centre the Earth. The $\hat{\boldsymbol{h}}$ axis is normal to the

[1] The Aries point is the intersection point between the celestial equator and the ecliptic, also called equinox, and corresponding to the spring equinox (March 21st).

orbit plane.The $\hat{\boldsymbol{\vartheta}}$ axis lies on the orbit plane, orthogonal to the two ones previously defined, and positively oriented towards the direction of motion [1] [6].

Target reference frame

The target reference frame, defined by orthogonal, right-handed triad $\hat{\mathbf{t}}_1, \hat{\mathbf{t}}_2, \hat{\mathbf{t}}_3$, such as:

$$\hat{\mathbf{t}}_1 \times \hat{\mathbf{t}}_2 = \hat{\mathbf{t}}_3 \tag{3-3}$$

is the reference frame representing the desired pointing [1] [6].

2.1.2. Attitude matrix

Let us consider a spacecraft as a rigid body identified by the body reference frame $\hat{\boldsymbol{\imath}}, \hat{\boldsymbol{\jmath}}, \hat{\boldsymbol{k}}$. The angular position relative to the Inertial Reference Frame $\hat{\mathbf{c}}_1, \hat{\mathbf{c}}_2, \hat{\mathbf{c}}_3$ can be defined by the attitude matrix $\mathbf{A}$ [1] [7].

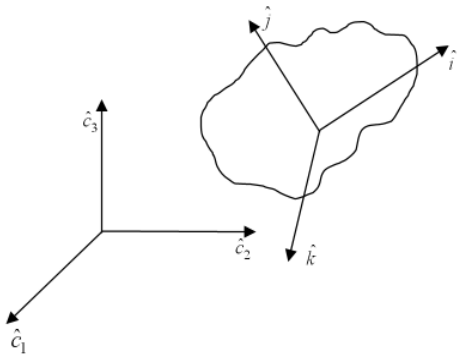

Fig. 7 – Body and Inertial Reference Frames

Consider a vector $\vec{\mathbf{v}}$, e.g. the spacecraft velocity vector. If $\vec{\mathbf{v}}$ and $\vec{\mathbf{v}}'$ are the Cartesian representation of the same vector in two different reference frames, then:

$$\vec{\mathbf{v}}' = \mathbf{A}\vec{\mathbf{v}} + \vec{\mathbf{s}} \tag{3-4}$$

where the vector $\vec{\mathbf{s}}$ represents the translation of the origin from the first reference frame to the second one, and $\mathbf{A}$ is the transformation matrix indicating the rotation of the axes between the two frames (called *Attitude Matrix* or *Direction Cosine Matrix*).

Considering the two frames centred in the same point (translation $\vec{\mathbf{s}} = \vec{\mathbf{0}}$), the vector $\vec{\mathbf{v}}$ can be written in the two reference frames:

$$\vec{\mathbf{v}} = \mathrm{X}\hat{\mathbf{c}}_1 + \mathrm{Y}\hat{\mathbf{c}}_2 + \mathrm{Z}\hat{\mathbf{c}}_3 = \mathrm{x}\hat{\mathbf{i}} + \mathrm{y}\hat{\mathbf{j}} + \mathrm{z}\hat{\mathbf{k}} \tag{3-5}$$

then, from calculus:

$$\begin{bmatrix} \mathrm{x} \\ \mathrm{y} \\ \mathrm{z} \end{bmatrix} = \begin{bmatrix} \hat{\mathbf{i}} \cdot \hat{\mathbf{c}}_1 & \hat{\mathbf{i}} \cdot \hat{\mathbf{c}}_2 & \hat{\mathbf{i}} \cdot \hat{\mathbf{c}}_3 \\ \hat{\mathbf{j}} \cdot \hat{\mathbf{c}}_1 & \hat{\mathbf{j}} \cdot \hat{\mathbf{c}}_2 & \hat{\mathbf{j}} \cdot \hat{\mathbf{c}}_3 \\ \hat{\mathbf{k}} \cdot \hat{\mathbf{c}}_1 & \hat{\mathbf{k}} \cdot \hat{\mathbf{c}}_2 & \hat{\mathbf{k}} \cdot \hat{\mathbf{c}}_3 \end{bmatrix} \begin{bmatrix} \mathrm{X} \\ \mathrm{Y} \\ \mathrm{Z} \end{bmatrix} = \mathbf{A} \begin{bmatrix} \mathrm{X} \\ \mathrm{Y} \\ \mathrm{Z} \end{bmatrix} \tag{3-6}$$

Therefore, the attitude matrix **A** is composed by the directional cosines between the two reference frames, i.e. the 9 scalar quantities:

$$\mathrm{A} = \begin{bmatrix} \hat{\imath} \cdot \hat{c}_1 & \hat{\imath} \cdot \hat{c}_2 & \hat{\imath} \cdot \hat{c}_3 \\ \hat{\jmath} \cdot \hat{c}_1 & \hat{\jmath} \cdot \hat{c}_2 & \hat{\jmath} \cdot \hat{c}_3 \\ \hat{k} \cdot \hat{c}_1 & \hat{k} \cdot \hat{c}_2 & \hat{k} \cdot \hat{c}_3 \end{bmatrix} \tag{3-7}$$

Because the matrix components derive from the unit vectors, **A** is an orthonormal matrix and has the following properties:

- Its inverse transformation matrix is equal to its transposed matrix:

$$\mathbf{A^{-1} = A^{T}} \tag{3-8}$$

- Its determinant is equal to 1:

$$\mathbf{det(A) = 1} \tag{3-9}$$

- Its eigenvalues have unit norm:

$$\mathbf{A}\boldsymbol{a_j} = \boldsymbol{\lambda_j a_j} \tag{3-10}$$

where $\boldsymbol{\lambda_j}$, $\boldsymbol{a_j}$ are respectively the eigenvalues and the eigenvectors.

2.2. Attitude determination methods

A recurrent problem in spacecraft attitude determination is to determine the attitude, in other worlds the attitude matrix **A**, from a set of vector measurements.

Given a set of observation (or measured) unit vectors $\widehat{\mathbf{W}}_1, \dots, \widehat{\mathbf{W}}_n$ and relative reference unit vectors $\widehat{\mathbf{V}}_1, \dots, \widehat{\mathbf{V}}_n$, which are n known directions in the reference coordinate systems, the problem of attitude determination is to solve:

$$\mathbf{A}\widehat{\mathbf{V}}_i = \widehat{\mathbf{W}}_i \qquad (i = 1, \dots, n) \qquad (3\text{-}11)$$

Because both measured and relative reference unit vectors are affected by errors, the solution of the attitude matrix **A** does not exist in general, even for $n = 2$.

A lot of studies have been done in order to improve the attitude estimate accuracy and to define faster algorithms capable to be implemented on-board of satellite. In this paragraph three different methods will be presented: TRIAD, q-method and QUEST.

2.2.1. TRIAD method

The TRIAD algorithm [1] [8] [9] is a deterministic method, based on the rotation matrix representation of the attitude. Given two non-parallel observation vectors $\widehat{\mathbf{W}}_1$ and $\widehat{\mathbf{W}}_2$, with their relative reference vectors $\widehat{\mathbf{V}}_1$ and $\widehat{\mathbf{V}}_2$, the solution of eq. (3-11) is the attitude matrix **A** that satisfies:

$$\begin{cases} \mathbf{A}\widehat{\mathbf{V}}_1 = \widehat{\mathbf{W}}_1 \\ \mathbf{A}\widehat{\mathbf{V}}_2 = \widehat{\mathbf{W}}_2 \end{cases} \tag{3-12}$$

Because the solution is over determined by the above equations, any two unit vectors we can define an orthogonal coordinate system with basic vectors $\hat{q}$, $\hat{r}$, $\hat{s}$ given by:

(for $\widehat{\mathbf{V}}_1$ and $\widehat{\mathbf{V}}_2$)

$$\hat{\mathbf{q}}_\mathbf{R} = \widehat{\mathbf{V}}_1 \tag{3-13a}$$

$$\hat{\mathbf{r}}_\mathbf{R} = \widehat{\mathbf{V}}_1 \times \widehat{\mathbf{V}}_2 \,/\, \left|\widehat{\mathbf{V}}_1 \times \widehat{\mathbf{V}}_2\right| \tag{3-13b}$$

$$\hat{\mathbf{s}}_\mathbf{R} = \hat{\mathbf{q}}_\mathbf{R} \times \hat{\mathbf{r}}_\mathbf{R} \tag{3-13c}$$

(for $\widehat{\mathbf{W}}_1$ and $\widehat{\mathbf{W}}_2$)

$$\hat{\mathbf{q}}_\mathbf{B} = \widehat{\mathbf{W}}_1 \tag{3-14a}$$

$$\hat{\mathbf{r}}_\mathbf{B} = \widehat{\mathbf{W}}_1 \times \widehat{\mathbf{W}}_2 \,/\, \left|\widehat{\mathbf{W}}_1 \times \widehat{\mathbf{W}}_2\right| \tag{3-14b}$$

$$\hat{\mathbf{s}}_{\mathbf{B}} = \hat{\mathbf{q}}_{\mathbf{B}} \times \hat{\mathbf{r}}_{\mathbf{B}} \tag{3-14c}$$

where the subscript $\boldsymbol{B}$ denote the measured vectors in the spacecraft body coordinates and the subscript $\boldsymbol{R}$ the observation vectors in the reference frame (e.g. the inertial reference frame). At given time, two measured vectors determine the body matrix $\mathbf{M}_{\mathbf{B}}$:

$$\mathbf{M}_{\mathbf{B}} = [\hat{\mathbf{q}}_{\mathbf{B}} \vdots \hat{\mathbf{r}}_{\mathbf{B}} \vdots \hat{\mathbf{s}}_{\mathbf{B}}] \tag{3-15}$$

and relative reference vectors in the reference frame, $\mathbf{M}_{\mathbf{R}}$:

$$\mathbf{M}_{\mathbf{R}} = [\hat{\mathbf{q}}_{\mathbf{R}} \vdots \hat{\mathbf{r}}_{\mathbf{R}} \vdots \hat{\mathbf{s}}_{\mathbf{R}}] \tag{3-16}$$

The attitude matrix **A** is given by eq. (3-11):

$$\mathbf{A}\mathbf{M}_{\mathbf{R}} = \mathbf{M}_{\mathbf{B}} \tag{3-17}$$

that can be solved for **A** to give:

$$\mathbf{A} = \mathbf{M}_{\mathbf{B}}\mathbf{M}_{\mathbf{R}}^{-\mathbf{1}} \tag{3-18}$$

Because $\mathbf{M_R}$ is orthogonal, then:

$$\mathbf{M_R^{-1}} = \mathbf{M_R^T} \tag{3-19}$$

and hence there exists a unique orthogonal matrix **A** which satisfy:

$$\mathbf{A} = \mathbf{M_B M_R^T} \tag{3-20}$$

The eq. (3-20) defines the **TRIAD solution**.

Note that inverse trigonometric functions are not required: a unique, unambiguous attitude is obtained and computation requirements are minimal. The simplicity of eq. (3-20) made it attractive for on-board processing. There are no requirements in the choice of the coordinate system for measured and observed vectors, but the only two requirements are:

1) $\mathbf{M_R}$ possess an inverse, which follows because for $\hat{\mathbf{V}}_\mathbf{1}$ and $\hat{\mathbf{V}}_\mathbf{2}$ are nonparallel, i.e.:

$$\left|\hat{\mathbf{V}}_\mathbf{1} \cdot \hat{\mathbf{V}}_\mathbf{2}\right| < \mathbf{1} \tag{3-21}$$

hence the unit vectors $\hat{\mathbf{q}}_{\mathbf{R}}$, $\hat{\mathbf{r}}_{\mathbf{R}}$ and $\hat{\mathbf{s}}_{\mathbf{R}}$ are linearly independent.

2) $$\hat{\mathbf{V}}_{\mathbf{1}} \cdot \hat{\mathbf{V}}_{\mathbf{2}} = \hat{\mathbf{W}}_{\mathbf{1}} \cdot \hat{\mathbf{W}}_{\mathbf{2}} \tag{3-22}$$

that is the necessary and sufficient condition for which the attitude matrix given by eq. (3-20) also satisfy eq. (3-12).

The TRIAD solution is not symmetric in indices 1 and 2. The preferential treatment of the vectors $\hat{\mathbf{V}}_{\mathbf{1}}$ and $\hat{\mathbf{W}}_{\mathbf{1}}$ in eq. (3-13a) and eq. (3-14a) over the vectors $\hat{\mathbf{V}}_{\mathbf{2}}$ and $\hat{\mathbf{W}}_{\mathbf{2}}$ suggest that $\hat{\mathbf{V}}_{\mathbf{1}}$ and $\hat{\mathbf{W}}_{\mathbf{1}}$ should be the more accurate measurements: this ensures that the attitude matrix $\mathbf{A}$ transforms $\hat{\mathbf{V}}_{\mathbf{1}}$ from the reference frame to the body frame exactly and vector $\hat{\mathbf{V}}_{\mathbf{2}}$ is used only to determine the phase angle about $\hat{\mathbf{V}}_{\mathbf{1}}$. This method identifies the attitude by first discarding part of measurements so that a solution exists. It is clear that a part of the information contained in the second vector is discarded. The discarded quantity is the measured component of $\hat{\mathbf{W}}_{\mathbf{2}}$ parallel to $\hat{\mathbf{W}}_{\mathbf{1}}$, i.e. $\hat{\mathbf{W}}_{\mathbf{1}} \cdot \hat{\mathbf{W}}_{\mathbf{2}}$. This measurement is coordinate independent, equals the known scalar $\hat{\mathbf{V}}_{\mathbf{1}} \cdot \hat{\mathbf{V}}_{\mathbf{2}}$ and is therefore useful for data validation (see eq. (3-22)). All of the error in $\hat{\mathbf{W}}_{\mathbf{1}} \cdot \hat{\mathbf{W}}_{\mathbf{2}}$ is assigned to the less accurate measurement $\hat{\mathbf{W}}_{\mathbf{2}}$, which accounts for the lost information.

TRIAD covariance matrix

The attitude covariance matrix is conventionally defined in terms of Euler angles. This computation is generally cumbersome and leads to have less information than the attitude covariance matrix referred to the body coordinate system. For this reason, the body-referenced covariance matrix will be first developed and then reported in terms of the Euler angles covariance matrix.

We first define the *error angle vector*, i.e. the set of small rotation angles carrying the true attitude matrix into the measured attitude matrix, as:

$$\boldsymbol{\delta\vartheta} = (\boldsymbol{\delta\vartheta_1} \quad \boldsymbol{\delta\vartheta_2} \quad \boldsymbol{\delta\vartheta_3})^{\mathbf{T}} \tag{3-23}$$

Thus, the body-referenced attitude covariance matrix is defined as:

$$\mathbf{P_{\vartheta\vartheta}} = \langle \boldsymbol{\delta\vartheta}\, \boldsymbol{\delta\vartheta}^{\mathbf{T}} \rangle \tag{3-24}$$

If we consider $\boldsymbol{\delta\vartheta}$ unbiased, then, for small errors, the true attitude matrix is:

$$\mathbf{A} = \begin{bmatrix} \mathbf{1} & \boldsymbol{\delta\vartheta_3} & \boldsymbol{-\delta\vartheta_2} \\ \boldsymbol{-\delta\vartheta_3} & \mathbf{1} & \boldsymbol{\delta\vartheta_1} \\ \boldsymbol{\delta\vartheta_2} & \boldsymbol{-\delta\vartheta_1} & \mathbf{1} \end{bmatrix} \langle \mathbf{A} \rangle \tag{3-25}$$

where $\langle \mathbf{A} \rangle$ is the expected value of $\mathbf{A}$, and the relative attitude covariance matrix is:

$$\mathbf{P} = \langle \boldsymbol{\delta A}\ \boldsymbol{\delta A^T} \rangle \tag{3-26}$$

where $\boldsymbol{\delta A} = \mathbf{A} - \langle \mathbf{A} \rangle$.

From eq. (3-25) and eq. (3-26), $\mathbf{P_{\vartheta\vartheta}}$ can be rewrote:

$$\mathbf{P_{\vartheta\vartheta}} = \left({}^{1}\!/_{2}\ \mathrm{tr}\,(\mathbf{P})\right)\mathbf{I} - \mathbf{P} \tag{3-27}$$

where tr ($\mathbf{P}$) denote the trace of $\mathbf{P}$ and $\mathbf{I}$ the identity matrix. The $\mathbf{P}$ matrix can be put in terms of observations and reference matrix $\mathbf{M_B}$ and $\mathbf{M_R}$. From eq. (3-20) [1]:

$$\mathbf{P} = \langle \boldsymbol{\delta M_B}\ \boldsymbol{\delta M_B^T} \rangle + \mathbf{A}\langle \boldsymbol{\delta M_R}\ \boldsymbol{\delta M_R^T} \rangle \mathbf{A^T} \tag{3-28}$$

or:

$$\mathbf{P} = \mathbf{P_{obs}} + \mathbf{A}\,\mathbf{P_{ref}}\,\mathbf{A^T} \tag{3-29}$$

Similarly, $\mathbf{P_{obs}}$ and $\mathbf{P_{ref}}$ can be rewritten as the sum of two terms, each generated by the variation of a single observation or reference vector.

2.2.2. *q-method*

The greatest drawback of the TRIAD method is that can accommodate only two observations. When more than two measurements are available, such as for the star trackers, these can be used only by cumbersomely combining the attitude solutions for the various observation vectors pairs. In addition, the TRIAD method is basically ad hoc, i.e. the measurements are combined to provide the attitude estimate, but this combination is not optimal in any statistical sense. Indeed, some accuracy is lost because part of measurement is discarded.

The *q-method* is an optimal algorithm derived by Davenport algorithm [10] [11].

Given a set of $n \geq 2$ measurement vectors $\mathbf{W_i}$ $(i = 1 \dots n)$ in the body coordinate system and relative reference vectors $\mathbf{V_i}$ $(i = 1 \dots n)$ in the reference coordinate system, an optimal attitude matrix **A** is offered by the minimization of the loss function:

$$\mathbf{J(A)} = \sum_{\mathbf{i=1}}^{\mathbf{n}} \boldsymbol{\omega_i} \left| \widehat{\mathbf{W}}_\mathbf{i} - \mathbf{A}\widehat{\mathbf{V}}_\mathbf{i} \right|^2 \tag{3-30}$$

where $\boldsymbol{\omega_i}$ is the weight of the *i-th* measurement vector.
If we consider the un-normalised vectors $\overrightarrow{\mathcal{W}_i}$ and $\vec{\mathcal{V}}_i$, defined as:

$$\overrightarrow{\boldsymbol{\mathcal{W}}}_\mathbf{i} = \sqrt{\boldsymbol{\omega_i}}\widehat{\mathbf{W}}_\mathbf{i} \tag{3-31}$$

$$\vec{\boldsymbol{\mathcal{V}}}_\mathbf{i} = \sqrt{\boldsymbol{\omega_i}}\widehat{\mathbf{V}}_\mathbf{i} \tag{3-32}$$

the loss function can be rewritten as:

$$\mathbf{J(A)} = -\mathbf{2} \sum_{\mathbf{i=1}}^{\mathbf{n}} \overrightarrow{\boldsymbol{\mathcal{W}}}_\mathbf{i} \, \mathbf{A} \, \vec{\boldsymbol{\mathcal{V}}}_\mathbf{i} + \textbf{constant terms} \tag{3-33}$$

The loss function $\mathbf{J}(\mathbf{A})$ is minimum when:

$$\mathbf{J}'(\mathbf{A}) = -\mathbf{2}\sum_{\mathbf{i=1}}^{\mathbf{n}} \vec{\boldsymbol{W}}_{\mathbf{i}}\,\mathbf{A}\,\vec{\boldsymbol{V}}_{\mathbf{i}} \equiv tr(\boldsymbol{W}^{\boldsymbol{T}}\mathbf{A}\boldsymbol{V}) \tag{3-34}$$

is maximum, i.e. the gain function $\boldsymbol{g}(\boldsymbol{A})$ is equal to:

$$\boldsymbol{g}(\boldsymbol{A}) = tr(\boldsymbol{W}^{\boldsymbol{T}}\mathbf{A}\boldsymbol{V}) \tag{3-35}$$

where $\boldsymbol{W}$ and $\boldsymbol{V}$ are $(3 \times n)$ matrices defined by:

$$\boldsymbol{W} \equiv \left[\vec{\boldsymbol{W}}_{\boldsymbol{1}} \vdots \vec{\boldsymbol{W}}_{\boldsymbol{2}} \vdots \cdots \vdots \vec{\boldsymbol{W}}_{\boldsymbol{n}}\right] \tag{3-35a}$$

$$\boldsymbol{V} \equiv \left[\vec{\boldsymbol{V}}_{\boldsymbol{1}} \vdots \vec{\boldsymbol{V}}_{\boldsymbol{2}} \vdots \cdots \vdots \vec{\boldsymbol{V}}_{\boldsymbol{n}}\right] \tag{3-35b}$$

A way to find $\mathbf{A}$, which maximizes the eq. (3-34), is to introduce the quaternion $\mathbf{q}$ and parameterize the attitude matrix as:

$$\mathrm{A}(\boldsymbol{q}) = (\mathrm{q}_4^2 - \mathbf{q}\cdot\mathbf{q})\mathbf{I} + 2\mathbf{q}\mathbf{q}^{\mathrm{T}} - 2\mathrm{q}_4\mathrm{Q} \tag{3-36}$$

where the quaternion $\boldsymbol{q}$ has been written in terms of its vector part $\mathbf{q}$ and scalar part q_4:

$$\boldsymbol{q} = \begin{pmatrix} \mathbf{q} \\ \mathrm{q}_4 \end{pmatrix} \tag{3-37}$$

I is the (3×3) identity matrix and Q is the skew-symmetric matrix:

$$Q = \begin{bmatrix} 0 & -\mathrm{q}_3 & \mathrm{q}_2 \\ \mathrm{q}_3 & 0 & -\mathrm{q}_1 \\ -\mathrm{q}_2 & \mathrm{q}_1 & 0 \end{bmatrix} \tag{3-38}$$

Substituting the eq. (3-36) in eq. (3-35):

$$\boldsymbol{g}(\boldsymbol{q}) = \boldsymbol{q}^{\mathrm{T}}\mathrm{K}\boldsymbol{q} \tag{3-39}$$

where K is the (4×4) matrix:

$$K = \begin{pmatrix} S - \boldsymbol{I}\sigma & Z \\ Z^T & \sigma \end{pmatrix} \tag{3-40}$$

with the components defined by:

$$B \equiv \mathcal{W}\mathcal{V}^T \tag{3-41a}$$

$$S \equiv B^T + B \tag{3-41b}$$

$$Z \equiv (B_{23} - B_{32} \quad B_{31} - B_{13} \quad B_{12} - B_{21})^T \tag{3-41c}$$

$$\sigma \equiv tr(B) \tag{3-41d}$$

The maximum of the eq. (3-39), subjected to the constraint $\boldsymbol{q}^T\boldsymbol{q} = 1$, can be found by means the Lagrange multipliers method. To proceed with this method, we have to define a new function:

$$g(\boldsymbol{q}) = \boldsymbol{q}^T K \boldsymbol{q} - \lambda \boldsymbol{q}^T \boldsymbol{q} \tag{3-42}$$

where $g(\boldsymbol{q})$ is maximized without constraints and λ is the Lagrange multiplier, chosen to satisfy the normalization constraint.

Differentiating the eq. (3-42) respect to $\boldsymbol{q}^T$ and setting the result equal to zero, the eigenvector equation is obtained:

$$K\boldsymbol{q} = \lambda \boldsymbol{q} \tag{3-43}$$

Thus, the quaternion which parameterizes the optimal attitude matrix, in the sense of eq. (3-30), is an eigenvector of *K*. Substituting the eq. (3-43) in eq. (3-39), we obtain:

$$\boldsymbol{g}(\boldsymbol{q}) = \boldsymbol{q}^T K \boldsymbol{q} = \boldsymbol{q}^T \lambda \boldsymbol{q} = \lambda \tag{3-44}$$

Hence, $g(\mathrm{A})$ is the maximum, if the eigenvector corresponds to the largest eigenvalue. It can be demonstrated that if at least two of the measured vectors $\mathcal{W}_i$ are not collinear, the eigenvalues of *K* are distinct and this method yields an unambiguous quaternion, i.e. the attitude. The q-method provides an optimal least-squares estimate of the attitude, given vector measurements in the body frame and information on those same vectors in the inertial reference frame. The key of this method is to solve for eigenvalues and eigenvectors of the **K** matrix. The major drawback of q-method is that requires to construct measurement vectors, not always possible, and weight the entire vector. An alternative method, based on q-method, which avoid the necessity for computing eigenvectors is the QUEST algorithm.

2.2.3. QUEST method

The QUEST (*QUaternion ESTimator*) algorithm is an alternative method, based on q-method, that provides a "cheaper" way to estimate the solution to the eigenproblem defined in eq. 3-43. Recalling that the least squares optimal attitude minimizes the loss function in q-method (see eq. (3-30)):

$$\mathbf{J(A)} = \sum_{\mathbf{i=1}}^{\mathbf{n}} \boldsymbol{\omega_i} \left| \widehat{\mathbf{W}}_\mathbf{i} - \mathbf{A}\widehat{\mathbf{V}}_\mathbf{i} \right|^{\mathbf{2}} \tag{3-45}$$

when maximizing the gain function (see eq. (3-35) and eq. (3-44)):

$$\boldsymbol{g(A)} = tr(\boldsymbol{\mathcal{W}^T \mathbf{A} \mathcal{V}}) \tag{3-46}$$

$$\boldsymbol{g(q)} = \boldsymbol{q}^T K \boldsymbol{q} = \boldsymbol{q}^T \lambda \boldsymbol{q} = \lambda \tag{3-47}$$

we can obtain, rearranging the last two equations:

$$\lambda_{opt} = \sum_{\mathbf{i=1}}^{\mathbf{n}} \boldsymbol{\omega_i} - \boldsymbol{J} \tag{3-48}$$

Since $\boldsymbol{J(A)}$ is small for the optimal eigenvalue, the eq. (3-48) can be approximated:

$$\lambda_{opt} \approx \sum_{\mathbf{i=1}}^{\mathbf{n}} \boldsymbol{\omega_i} \tag{3-49}$$

From eq. (3-49), the value of corresponding eigenvector can be calculated.

Part II

Autonomous on-orbit calibration

3

Calibration Process

3.1. Introduction

Star Trackers are considered among the most accurate attitude sensors, and have been traditionally part of the avionics of expensive, high level spacecraft. Such a trend is currently changing, with the availability of a generation of not so expensive products devoted to middle class platforms. There is even some research effort aimed to obtain very low cost COTS (component-off-the-shelf) based devices suitable for nanosatellites and cubesat ([12] [13] [14]). The limitation in the final device cost involves a significant reduction in the production process, especially involving the test and calibration phase. Traditionally, high-end sensors devoted to important scientific missions go through a time-consuming, sophisticated calibration campaign which used specific test benches. This approach changes for the newly introduces class of devices, both for the costs involved as well as for the far shorter time-to-market required for batches of several

tens of sensors. Moved from commercial reasons, designers reconsidered the motivation for the test campaigns, and attempted to obtain a basic accuracy from the batch of instruments, leaving for in-flight operations the final validation of the single sensor. Basically there is a shift from the idea of crafting a state-of-art, as-perfect-as-possible instrument, to the concept of a device which is in some way tuneable during its operational lifetime, in order to accommodate minor issues deriving from a simpler manufacturing process. In such a way it is possible to reduce the calibration at the factory and to directly evaluate the performance once in orbit. Indeed, small deviations in the equipment occurring during the most critical condition, i.e. the launch phase, can be still corrected before real measurements campaign will begin. Clearly this approach becomes extremely interesting for the new instruments built in large batches for huge Low Earth Orbit formations' satellites.

On the other hand, it is difficult to argue that optoelectronics had dramatic advances in recent years. CCD-based sensors met a significant evolution, also fed by huge terrestrial, consumer electronics commercial markets. As a result, instruments based on CCD miniature cameras have been proposed for a host of space-related applications, including lab hardware close to star trackers [15]. Additional uses encompassed on-board monitoring of

structural deformations (an application with heavy requirements in terms of refresh rate and data flow, [16], as well as short distance kinematic state determination (i.e. relative navigation) between spacecraft flying in formation [17]. To be noticed that navigation can be also performed by optoelectronic combined sensors having a significant portion of components in common with a star tracker [18]. Clearly all these applications, presenting the same calibration issues as per previous discussion, should have a benefit from the studies and the possible advances in the field. The advent of C-MOS based sensors as the APS resulted in an increase of the performance (not only in terms of accuracy, but also in terms of robustness to radiation) and paved the way to adoption of imaging sensors in many more missions, and also in multiple spacecraft formations, with further interest to effective calibration procedures [19].

The in-orbit calibration was first introduced in scientific mission requiring an extremely high accuracy, so that the pre-launch calibration was not deemed enough (as in the case of Herschel Space Observatory telescope, 2009). On the other hand, the in orbit calibration can be considered also a complement to an initial, simplified and coarse calibration performed on ground in order to limit or reduce the cost of that expensive (in terms of time and cost) operation. Nowadays, on-board calibration becomes

extremely appealing while dealing with large batches of medium quality sensors, as the ones accommodated on large formations and constellations, which numbers clearly do not fit extended test campaigns at the manufacturing sites. A clear interest to make available a re-calibration process arises and, as a result, autonomous calibration techniques - to be directly carried on during the flight - are an active field of research.

The topic of the following paragraphs is the on-orbit calibration of the star trackers. The approach, implemented through numerical simulations, follows the path already assessed in literature for a two-steps star tracker calibration [20] [21], also supported by analyses carried out with real space mission data [22].

3.2. Calibration Process

The proposed calibration method is used to estimate the main parameters influencing the performances of the star tracker:

- Focal length (f)
- Principal point offset (x_0, y_0) (*or bore sight error*)
- Focal plane distortions

This method can be applied both on-ground and on-orbit and the calibration parameters will be estimated through the star tracker image frames, where the stars have been identified manually or by means of dedicated algorithms robust to the calibration errors.

The optics of the camera has been modelled using the modelling of the pin-hole.

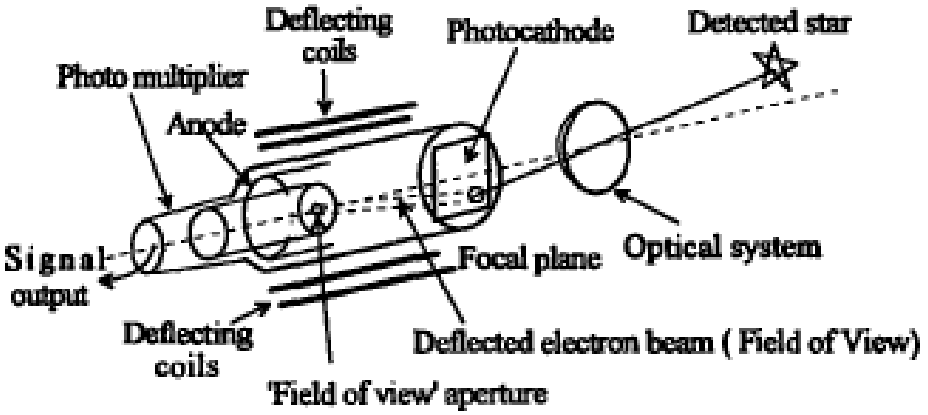

Fig. 8 – Star Tracker modelling [1] [6]

The method is composed by three main parts:

- A "raw" calibration on-ground of the focal length and principal point offset, that will be used as input for the on-orbit calibration;
- A "fine" calibration on-orbit of focal length and bore sight error, taking into account the previous ones;
- A "fine" calibration on-orbit of the focal plane distortion.

For what concerns the on-ground calibration, it is not foreseen any laboratory or dedicated optical tools for the calibration activities, but only night sky tests or the use of simulated (i.e. computer-generated) images of a portion of the sky. In this way it is possible to save costs and time.

The idea is to have a "raw" calibration of the star tracker on-ground, because the night sky tests are affected by the errors due to the presence of the atmosphere and no calibration of focal plane distortions or mechanical misalignments is done, and then, to perform a "fine" calibration once the spacecraft is in its orbit. Indeed, the main stresses on the star tracker, that can affect its calibration, are during the launch and, in addition, the effect on the focal length of the in-orbit change of temperature has to be considered. For this reason, we can consider the star tracker in this phase as in its operative "final" configuration and we can calibrate it, taking into account all effects (misalignments of the detector and the optical elements, distortions of the lens, defeats, …) that affect the performance of the sensor.

The calibration process is composed by:

- On-ground calibration:

  The standard non-linear least square optimal estimation (LS). This method is optimal in statistics sense, but required no limitation in computing and all of the measurements must first be collected before an estimate can be made [23]. This method is generally not used in real-time operations. Indeed, a batch of measurements is collected and used to estimate the parameters.

- On-orbit calibration:

  A combination of Least-Squares (LS) and Kalman filter (KF). This method may fulfill real-time computation constraints. For each set of measurements, LS provides the "raw" estimate of focal length and bore sight error as input of the KF, that provides a "fine" calibration taking into account the previous estimates. In parallel an estimation of focal plane distortions is done.

The method is based on the use of residuals between the directional cosines of the measured stars and corresponding stars in the on-board catalogue.

In other words, if the star tracker is not affected by errors:

$$\hat{v}_i^T \hat{v}_j = \hat{w}_i^T \hat{w}_j \tag{4-1}$$

where $\hat{w}_i$ is the unit vector that identified the i-th star measured (i.e. detected) by the sensor and $\hat{v}_i$ the relative catalogued star.

Otherwise:

$$\hat{v}_i^T \hat{v}_j - \hat{w}_i^T \hat{w}_j = R \tag{4-2}$$

where **R** is the vector including the residuals.

Because the inter-star angles are invariant of the rotational transformation, the eq. (4-1) is valid for any reference frame. Therefore, the knowledge of the spacecraft attitude is not necessary.

3.3. On-ground calibration

The aim of the on-ground calibration is to estimate the focal length (f) and the bore sight error (x_0, y_0) in order to have an initial

"raw" calibration of the sensor's focal plane. Otherwise, the star tracker could not identify the detected stars, and hence, not estimate the attitude for the spacecraft. In other words, the (positions of the) "imaged" stars have to be modified considering the principal point offset and the correction on $\boldsymbol{f}$. These calibration parameters will be used as input for the on-orbit calibration.

The initial on-ground calibration mimics the sensor's functioning like in space and is done using images of a portion of the sky coming from a simulation or night sky test. The information coming from the images are related to the components of the measured stars unit vector $\hat{w}$.

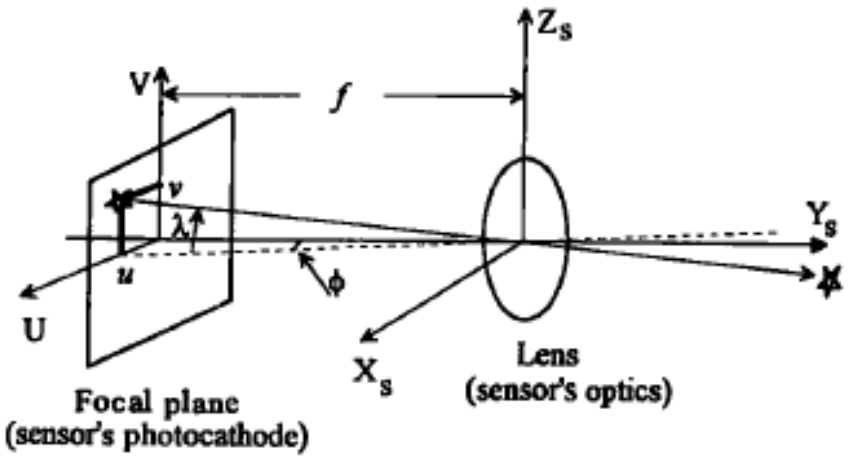

Fig. 9 – Star projection on the focal plane [1] [6]

In detail, the pinhole mode can be adopted, with the input data given by the bi-dimensional location of the image-point corresponding to the star in image of the detector (see Fig. 9).
Indeed, the components in the body reference frame of unit vector which is parallel to the line-of-sight of a given star can be obtained by:

$$\widehat{w} = \frac{1}{\sqrt{(x-x_0)^2+(y-y_0)^2+f^2}} \begin{bmatrix} -(x-x_0) \\ -(y-y_0) \\ f \end{bmatrix} \quad (4\text{-}3)$$

where f is the focal length and (x_0, y_0) is the optical centre of the image, i.e. the position (in pixels or in millimetres) where a star which is exactly located on the optical axis would be represented. The parameters f, x_0 and y_0 should be a priori known with a great accuracy, while their actual value depend on slight modifications occurred in the manufacturing process and on the effects of the environment (thermal and vibration induced stress) before, during and after the launch.

The measured unit vector can be compared with its relative inertial catalogued star unit vector $\hat{v}$, defined by:

$$\hat{v} = \begin{bmatrix} cos\alpha\ cos\delta \\ sin\alpha\ cos\delta \\ sin\delta \end{bmatrix} \tag{4-4}$$

where α is the right ascension and δ the declination as indicated in the catalogue.

While the $\hat{w}$ and $\hat{v}$ are referred two different coordinates systems (the body and inertial frame respectively), their inter-star angles are invariant and can be compared, as in the following:

$$\hat{\mathrm{v}}_{\mathrm{i}}^{\mathrm{T}}\hat{\mathrm{v}}_{\mathrm{j}} = \hat{\mathrm{w}}_{\mathrm{i}}^{\mathrm{T}}\hat{\mathrm{w}}_{\mathrm{j}} \tag{4-5}$$

where the subscripts i and j indicate the *i-th* and *j-th* stars. Substituting the relation (4-3) for the sensor's measurements, the eq. (4-5) becomes:

$$\hat{\mathrm{v}}_{\mathrm{i}}^{\mathrm{T}}\hat{\mathrm{v}}_{\mathrm{j}} = \frac{N}{D_1 D_2} = h\left(\hat{x}_0, \hat{y}_0, \hat{f}\right) \tag{4-6}$$

where:

$$\begin{cases} N = (x_i - x_0)\left(x_j - x_0\right) + (y_i - y_0)\left(y_j - y_0\right) + f^2 \\ D_1 = \sqrt{(x_i - x_0)^2 + (y_i - y_0)^2 + f^2} \\ D_2 = \sqrt{\left(x_j - x_0\right)^2 + \left(y_j - y_0\right)^2 + f^2} \end{cases} \tag{4-7}$$

The idea is to identify the values for the unknowns which minimize the residuals, as per the classical Least Squares estimator. Therefore, defining the estimates for (x_0, y_0, f) as:

$$\left(\hat{x}_0, \hat{y}_0, \hat{f}\right) \tag{4-8}$$

and the errors relevant to these estimates as:

$$(\Delta x_0, \Delta y_0, \Delta f) \tag{4-9}$$

the parameter will be represented as:

$$\begin{cases} x_0 = \hat{x}_0 + \Delta x_0 \\ y_0 = \hat{y}_0 + \Delta y_0 \\ f = \hat{f} + \Delta f \end{cases} \tag{4-10}$$

The substitution of eq. (4-10) in eq. (4-6) yields:

$$\hat{v}_i^T \hat{v}_j = h_{ij}\left(\hat{x}_0, \hat{y}_0, \hat{f}\right) + \begin{bmatrix} \frac{\partial h_{ij}}{\partial x_0} & \frac{\partial h_{ij}}{\partial y_0} & \frac{\partial h_{ij}}{\partial f} \end{bmatrix} \begin{bmatrix} \Delta x_0 \\ \Delta y_0 \\ \Delta f \end{bmatrix} \tag{4-11}$$

so that the residuals will read as:

$$R_{ij} = \hat{v}_i^T \hat{v}_j - h_{ij}(\hat{x}_0, \hat{y}_0, \hat{f}) = \begin{bmatrix} \frac{\partial h_{ij}}{\partial x_0} & \frac{\partial h_{ij}}{\partial y_0} & \frac{\partial h_{ij}}{\partial f} \end{bmatrix} \begin{bmatrix} \Delta x_0 \\ \Delta y_0 \\ \Delta f \end{bmatrix} \quad (4\text{-}12)$$

where:

$$J_{ij} = \begin{bmatrix} \frac{\partial h_{ij}}{\partial x_0} & \frac{\partial h_{ij}}{\partial y_0} & \frac{\partial h_{ij}}{\partial f} \end{bmatrix} \quad (4\text{-}13)$$

Iterating for n angular measurements:

$$\{\mathrm{R}\} = [\mathrm{J}]\{\Delta \mathrm{Z}\} \quad (4\text{-}14)$$

where:

$$\{R\} = \begin{Bmatrix} R_{12} \\ R_{13} \\ \vdots \\ R_{n-1,n} \end{Bmatrix} \quad (4\text{-}14a)$$

$$[\mathrm{J}] = \begin{bmatrix} \frac{\partial h_{12}}{\partial x_0} & \frac{\partial h_{12}}{\partial y_0} & \frac{\partial h_{12}}{\partial f} \\ \frac{\partial h_{13}}{\partial x_0} & \frac{\partial h_{13}}{\partial y_0} & \frac{\partial h_{13}}{\partial f} \\ \vdots & \vdots & \vdots \\ \frac{\partial h_{n-1,n}}{\partial x_0} & \frac{\partial h_{n-1,n}}{\partial y_0} & \frac{\partial h_{n-1,n}}{\partial f} \end{bmatrix} \tag{4-14b}$$

$$\{\Delta Z\} = \begin{Bmatrix} \Delta x_0 \\ \Delta y_0 \\ \Delta f \end{Bmatrix} \tag{4-14c}$$

for $(i = 1, \dots, n-1)$ and $(j = i+1, \dots, n)$, to identify a solution for the errors on the parameters:

$$\{\Delta Z\}_k = [J_k^T J_k]^{-1} J_k^T \{R\}_k \tag{4-15}$$

where $(k = 1,2, \dots, N)$ and $\boldsymbol{N}$ number of iterations, with the overall flowchart of the on-ground calibration algorithm reported in the following figure.

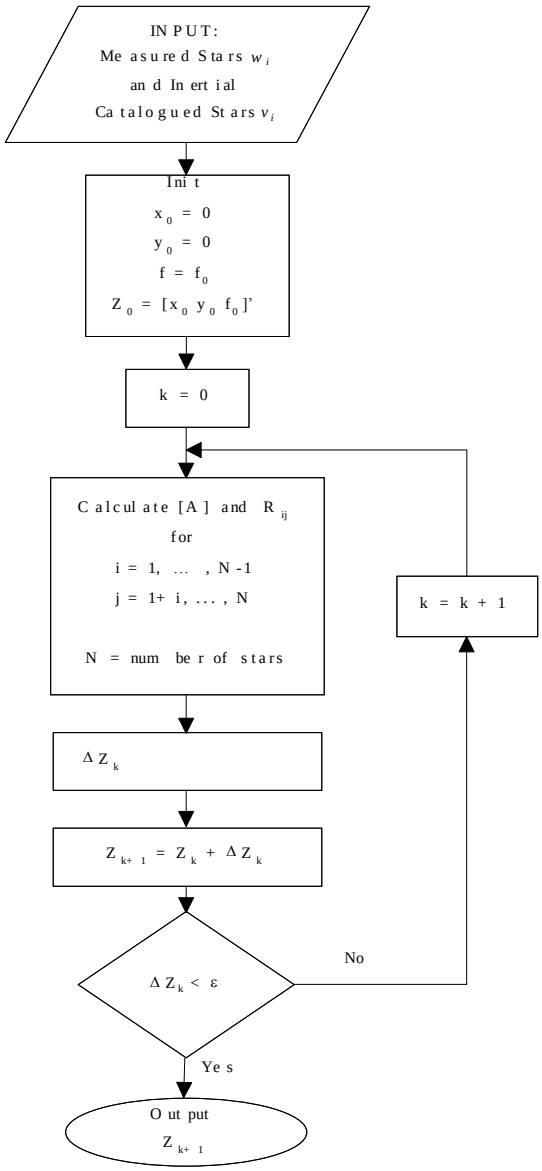

Fig. 10 – Flowchart of the on-ground calibration algorithm.

3.4. On-orbit calibration

Once the star tracker is in orbit the calibration problem is not anymore a static one, and – at least in theory – an ever improving calibration could be found by adding new measurements relevant to new stars. The dynamic nature can be exploited by the use of estimators like Kalman filters, largely adopted in the aerospace field [24], [25] and specifically in the attitude determination using star tracker [26] and even in the star-trackers algorithms themselves [27]. The use of recursive estimators, as opposed to batch Least Squares methods, provides significant advantages in terms of the data storage and computational resources required on-board the spacecraft.

This specific application of the Kalman filter leads to some interesting implementation issue. Notice that the number of measurements available at each step can vary, due to the number of stars recognized in each image. Such an issue is usually well managed by Kalman algorithm with its multi-input structure, by just voiding some observation matrix line. In the specific case however this change in size can be significant, leading to an unnecessary over-sizing of the variables. Not to say that large size of the observation matrix makes the Kalman loop expensive from the computational point of view and prone to ill-conditioning

issues in the repetitive operations with matrices. There is also an issue which has been represented in literature due to the linearization process of the observation matrix (equivalent to the J matrix in eq. (4-14). According to Samaan et al. [22] the application of an extended Kalman filter to images captured by the sensor can lead to divergence.

To this aim, following the approach outlined in [22], a two steps technique can be envisaged to process on-orbit measurements. A Least Square (LS) method is first applied to each single image including n stars above the threshold, working on the n!/2/(n-2)! inter stellar angles as inputs and providing as output the values for the offset of the principal point and the error on the focal length best fitting that specific image. Then a linear Kalman Filter works on the sequence in time of the calibration parameters gathered from the series of images, in order to reconstruct the behaviour of the sensor.

The dynamic process in the Kalman algorithm can be assumed as a static one, so that the state:

$$\{X\}_k = \begin{Bmatrix} \Delta x_0 \\ \Delta y_0 \\ \Delta f \end{Bmatrix} \tag{4-16}$$

is predicted to be constant in time. The associated covariance matrix is fed by the noise assumed for the process. The Kalman gain can be computed as:

$$K_k = P_k H_k^T [H_k P_k H_k^T + R_k]^{-1} \quad (4\text{-}17)$$

The observation equation is fed by the output of the Least Square method, and ends up to be the identity matrix:

$$H_k = \left[\frac{\partial Z_k}{\partial x_0} \quad \frac{\partial Z_k}{\partial y_0} \quad \frac{\partial Z_k}{\partial f}\right] = I_{3x3} \quad (4\text{-}18)$$

(in such a way, the risk of false identification in the single image is limited and the process itself becomes more robust).
The final estimate results from the blending of prediction and measurements, as:

$$X_{k+1} = X_k + K_k[Z_k - H_k X_k] \quad (4\text{-}19)$$

The filter computes an improved evaluation of the calibration parameters as the time goes on and new images are acquired and processed by the star tracker. The convergence of the filter is

expected to be fast due to the usual extremely limited magnitude of the errors. Notice that in such a way it could be possible to investigate the behaviour in time of the sensor and evaluate the shift of calibration parameters in presence of perturbations, such as temperature changes.

Following Fig. 11 reports the flowchart of the algorithm to be applied for the in-orbit calibration. These algorithms are built in such a way to take into account the limitations in the on-board computational capabilities, as “batch” computation performed by Least Squares method is limited to the single image. Instead Kalman Filter, as every recursive filter, moves on from a step to the next one by storing only the more recent value for the estimates and the associated covariance matrix (which in the present case is a 3x3 matrix).

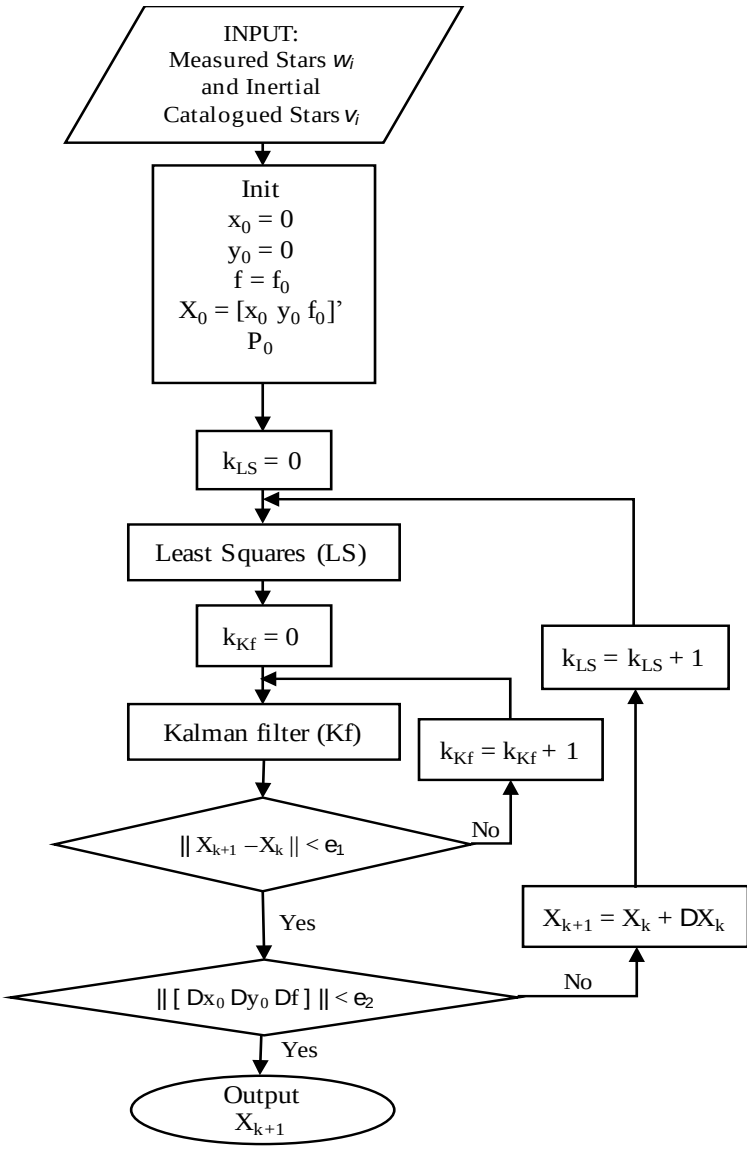

Fig. 11 – Flowchart of principal point and focal length estimation carried on during the in-orbit calibration phase.

3.4.1. Cases study

The study of the calibration algorithms has been performed using a simulated star tracker in MatLab, with the following (nominal) characteristics:

- CCD size = (1024x1024) pixels
- pixel size = 0.018 mm
- focal length (f) = 51.7 mm
- offset ($x_0 = 0\ pixel, y_0 = 0\ pixel$)
- maximum number of tracked stars (N_{max}) = 15

In the real application, the instrument's nominal characteristics will end up to be different from the actual ones, due to slight misalignments or manufacturing issues (therefore the need for calibration). For this reason we consider that, after the manufacturing, the star tracker has a slight error on principal point offset and focal length computed by the on-ground calibration algorithm:

- focal length (f) = 51.8 mm
- offset ($x_0 = 1\ pixel, y_0 = -1\ pixel$)

Moreover we consider that the measurements are affected by Gaussian white noise.

In the following are reported the analyses performed on different in-flight cases, i.e. with different errors on offset and focal length, where the on-orbit calibration algorithm has been applied. For all cases we consider the same on-ground calibration parameters previously reported.

CASE STUDY #1

The simulation has been performed considering a slight error in principal point offset and focal length and no distortions affecting the focal plane. The values of that parameters, after the in-flight phases, are:

- focal length (f) = 51.9 mm
- offset ($x_0 = 1.1\ pixel, y_0 = -0.9$)

For the simulation the parameters used as input for the on-orbit calibration algorithm are:

- focal length (f) = 51.8 mm
- offset ($x_0 = 1\ pixel, y_0 = -1\ pixel$)
- number of tracked stars N = 15
- duration of the simulation t = 10 s (100 photograms)

where f and (x_0, y_0) values come from the on-ground calibration.

Results CASE STUDY #1

In the following figures are reported the results of the simulation in a realistic noise perturbed case.

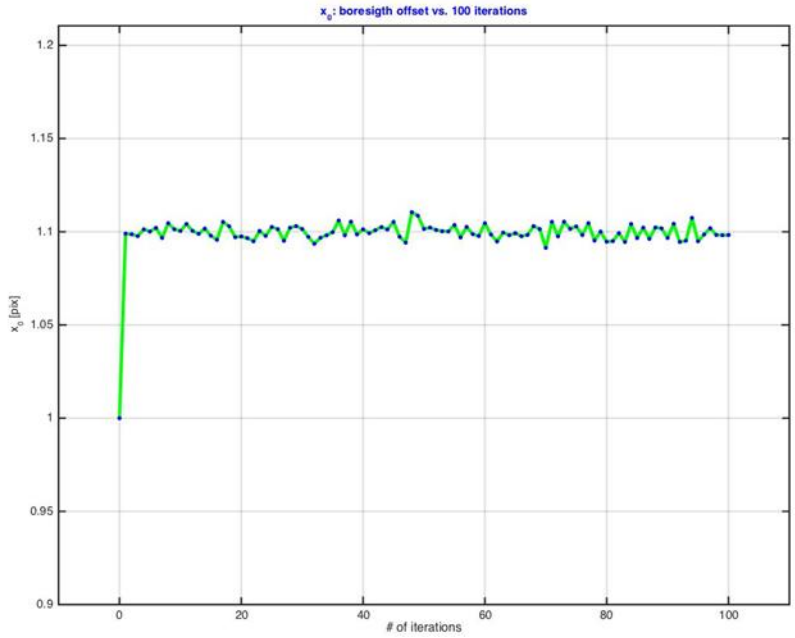

Fig. 12 – Filter results in a realistic noise perturbed case: x_0 [pix].

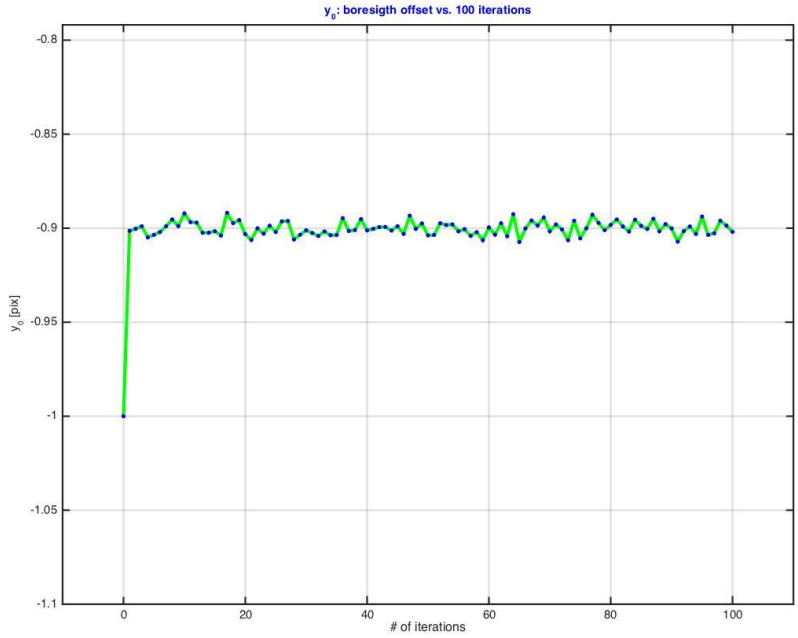

Fig. 13 – Filter results in *a realistic noise perturbed case*: y_0 [pix]

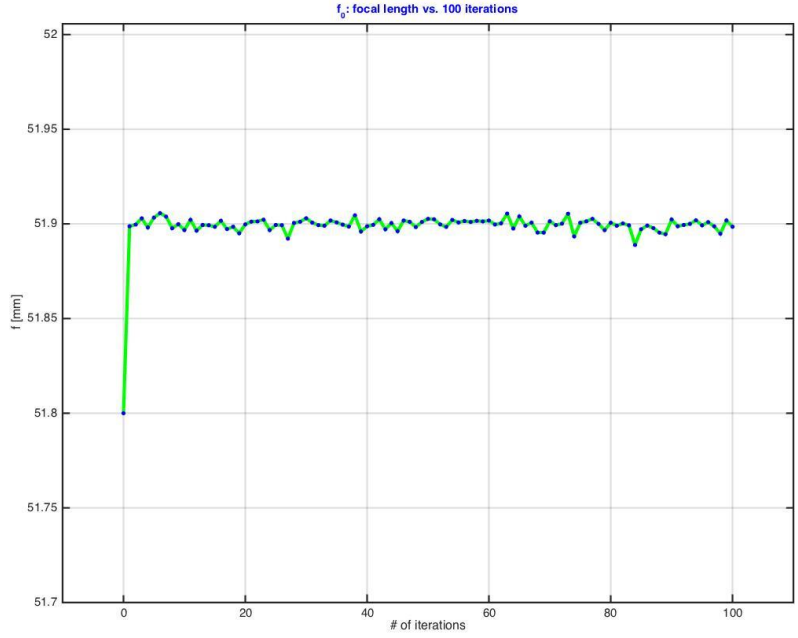

Fig. 14 – Filter results in *a realistic noise perturbed case*: f [mm]

The above graphs show as the algorithm is able to recover to the actual values of offset and focal length after few cycles.

CASE STUDY #2

This simulation takes into account heavy errors in the offset and focal length. The actual values, after the in-flight operations are:

- focal length (f) = 53.0 mm
- offset ($x_0 = 15\ pixels, y_0 = 1\ pixel$)

The initial conditions and the simulation duration for that case study is the same of the previous one.

Results of CASE STUDY #2

In the following are shown the results of the on-orbit calibration parameter.

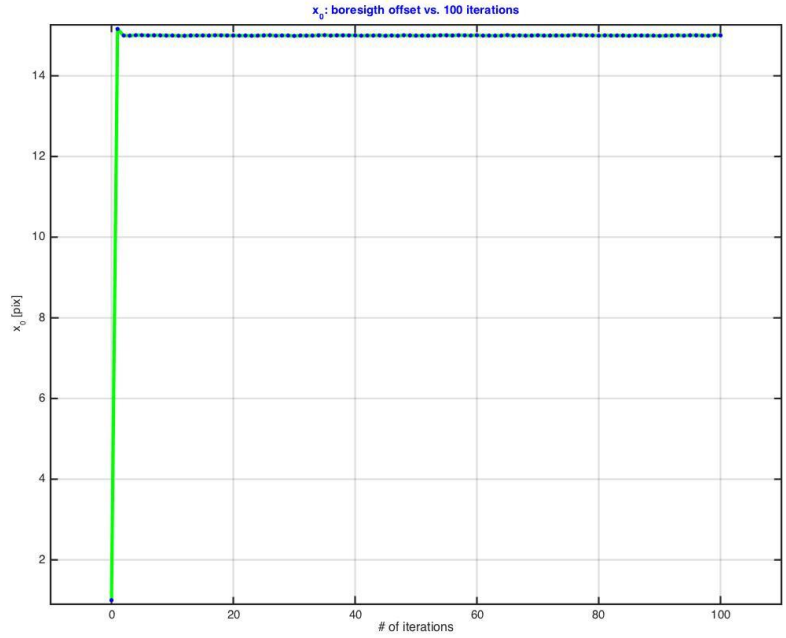

Fig. 15 – Filter in a realistic noise perturbed case: x_0 [pix].

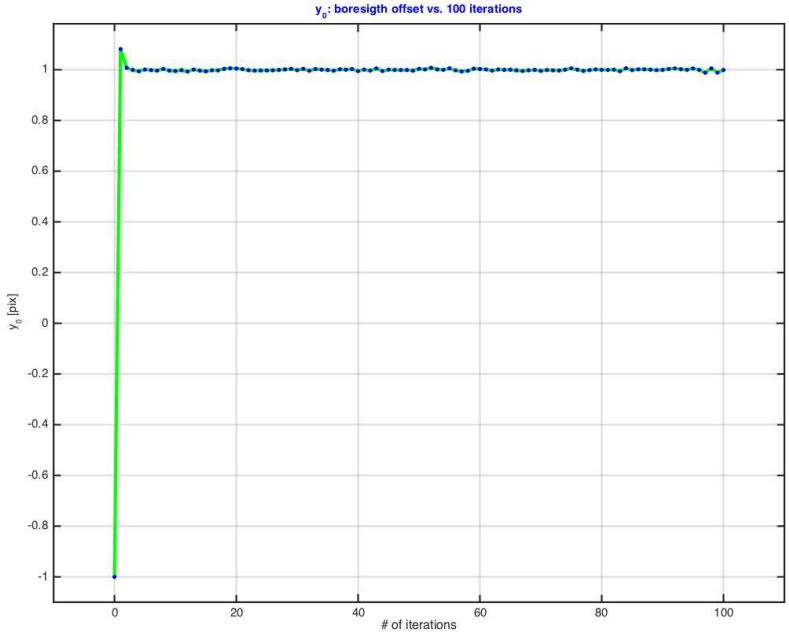

Fig. 16 – Filter results in a realistic noise perturbed case: y_0 [pix].

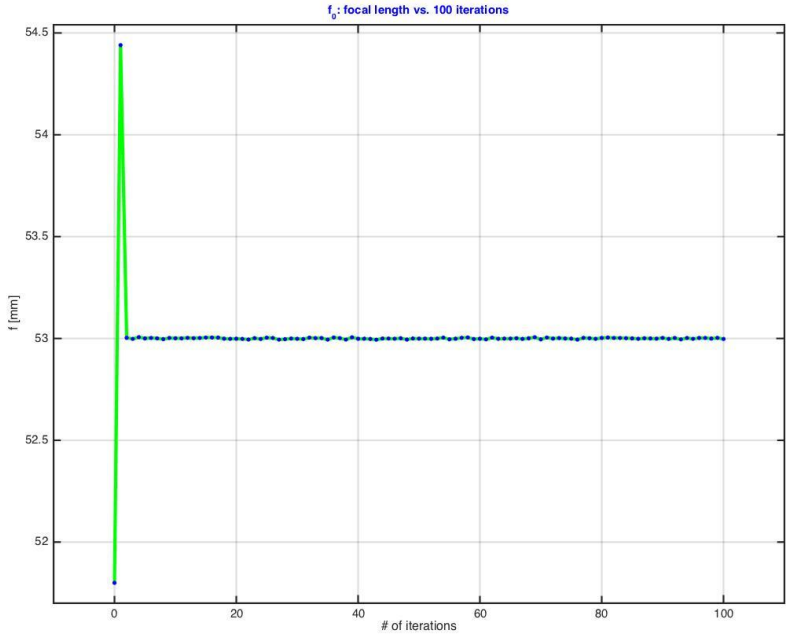

Fig. 17 – Filter results in a realistic noise perturbed case: f [mm]

Also in this case, where the measurements are affected heavy errors on initial calibration parameters, the algorithm is able to compute the actual offset and focal length values.

CASE STUDY #3

In this simulation we consider a portion of sky populated by few stars. The star tracker is affected by slight errors on focal length and offset (as for case study #1). The number of tracked stars is N = 5. Also for that case study, the on-ground parameters have been

used as input for the on-orbit calibration algorithm and duration of simulation is 60 s.

Results of the CASE STUDY #3

In the following are reported the results of the simulation.

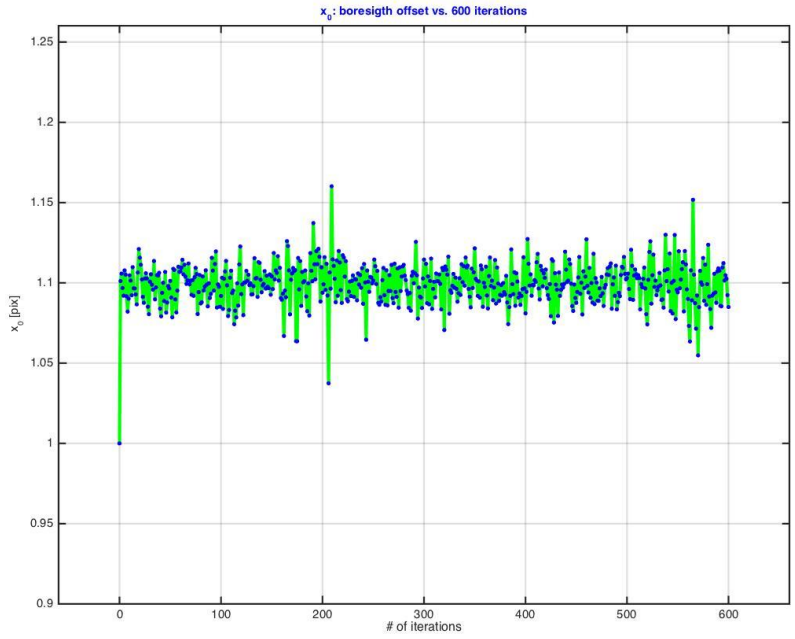

Fig. 18 – Filter results in a realistic noise perturbed case: x_0 [pix]

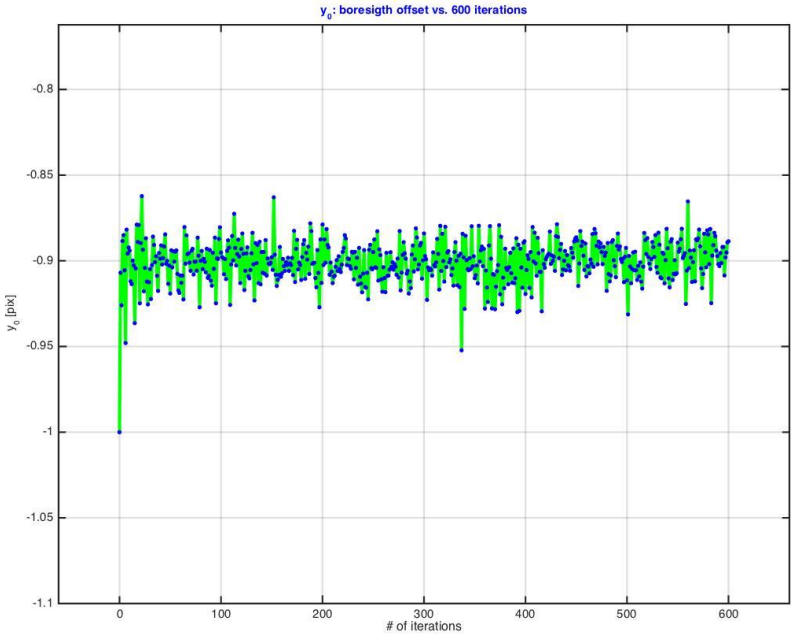

Fig. 19 – Filter results in a realistic noise perturbed case: y_0 [pix]

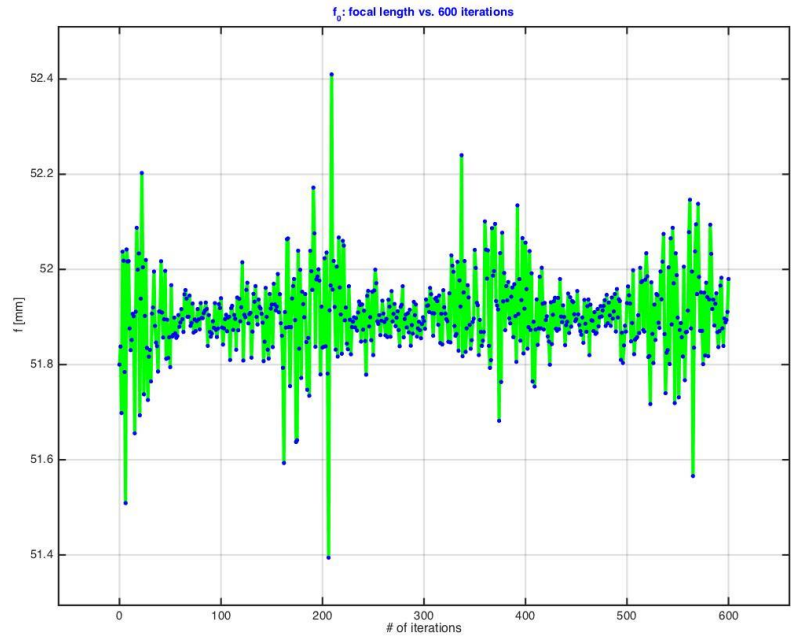

Fig. 20 – Filter results in a realistic noise perturbed case: f [mm]

The figures shown that the filter is able to compute the calibration parameters, but the standard deviation on the offset and focal length values increases due to the reduction of tracked stars, i.e. of the available measurements.

CASE STUDY #4

In the case, we consider the same conditions of CASE STUDY #2 with only exception that there are few tracked stars ($N = 5$) and the duration of the simulation is t = 60 s.

Results of the CASE STUDY #4

The results of case study #4 are reported in the following graphs.

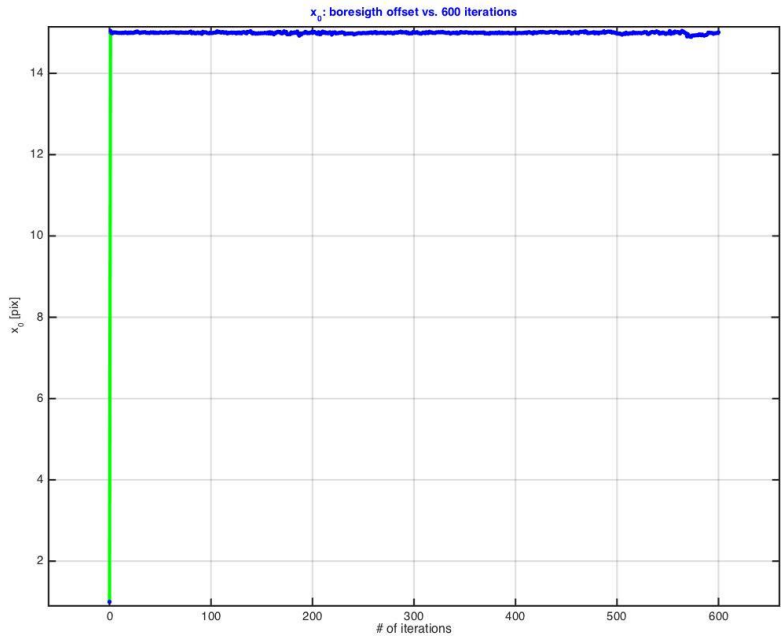

Fig. 21 – Filter results in a realistic noise perturbed case: x_0 [pix].

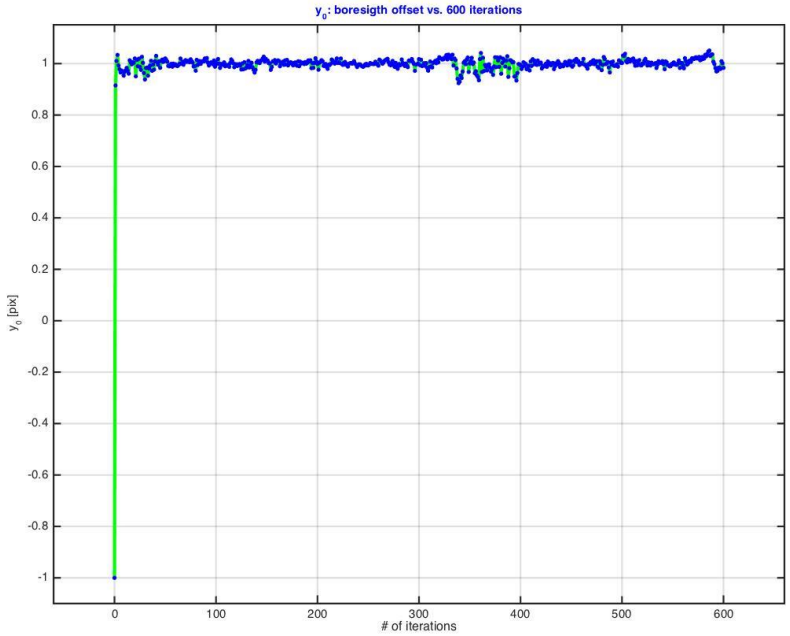

Fig. 22 – Filter results in a realistic noise perturbed case: y_0 [pix].

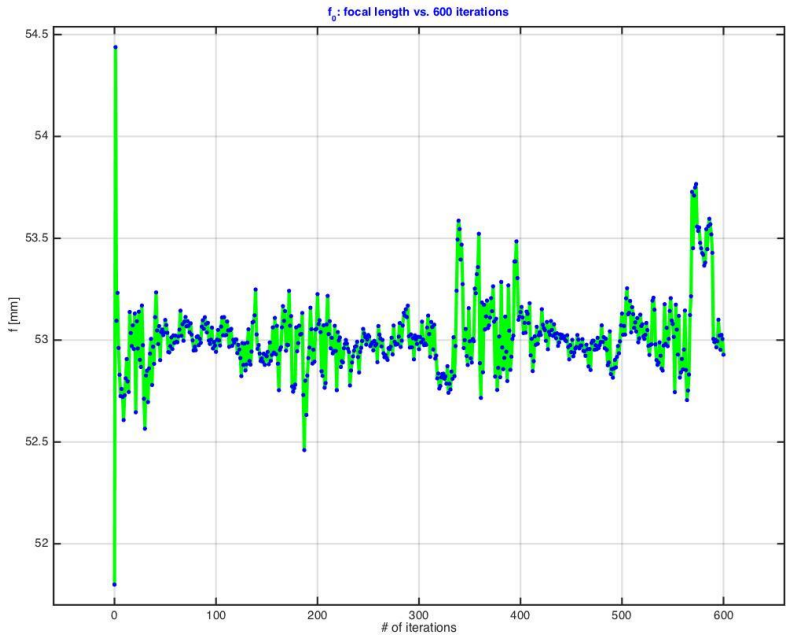

Fig. 23 – Filter results in a realistic noise perturbed case: f [mm]

Also in this case, the filter is able to compute the calibration parameters. The figures show that the standard deviation increases due to the low number of tracked stars, especially for the focal length value.

CASE STUDY #5

In that case study, it has been considered a case where the star tracker has affected by slight errors and detects false stars during the calibration. The initial conditions are:

- focal length (f) = 53.0 mm
- offset ($x_0 = 0\ pixel, y_0 = 0\ pixel$)
- number of tracked stars N = 15

The simulation has been performed in the ideal case (without noise on the measurements) and the "actual" case (with measurements affected by noise).

Results of CASE STUDY #5

Starting from the parameters computed during the on-ground calibration, Fig. 24 shows that the application of the on-orbit calibration algorithm in the ideal case of noiseless measurements.

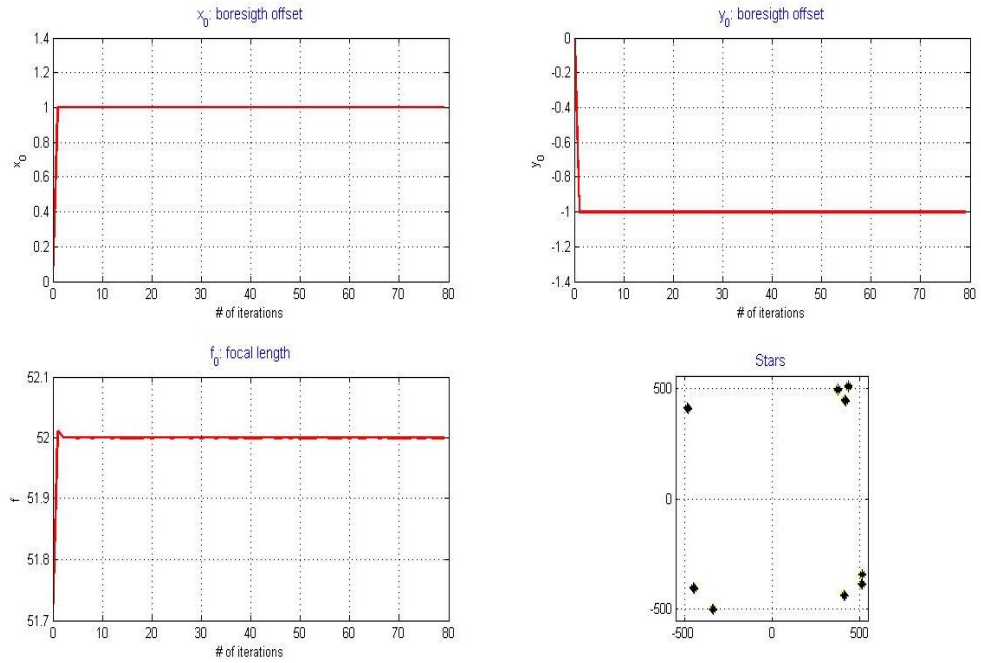

Fig. 24 – Filter results in an ideal (without noise) case.

The results are x0 = 1 pixel, y0 = -1 pixel for the principal point offset, and f0 = 52.0 mm for the focal length. These values perfectly agree with the inaccuracies that have been purposely included in the simulation.

Notice that the in orbit calibration phase has been simulated by considering a slowly moving point of view and a slow rotation of the spacecraft, resulting in a slight change of the image of the portion of the sky. These parameters affect the generation of the images and their identification with catalogue data, and do not enter directly in the calibration algorithm.

Real world sensors obviously add some noise to the measurements. Fig. 25 represents this scenario, showing that the algorithms is still perfectly managing this case, when the noise added has a standard deviation in the order of 0.1 pixels for the principal point offset and 0.01 mm for the focal length (i.e. 1/10 of the error).

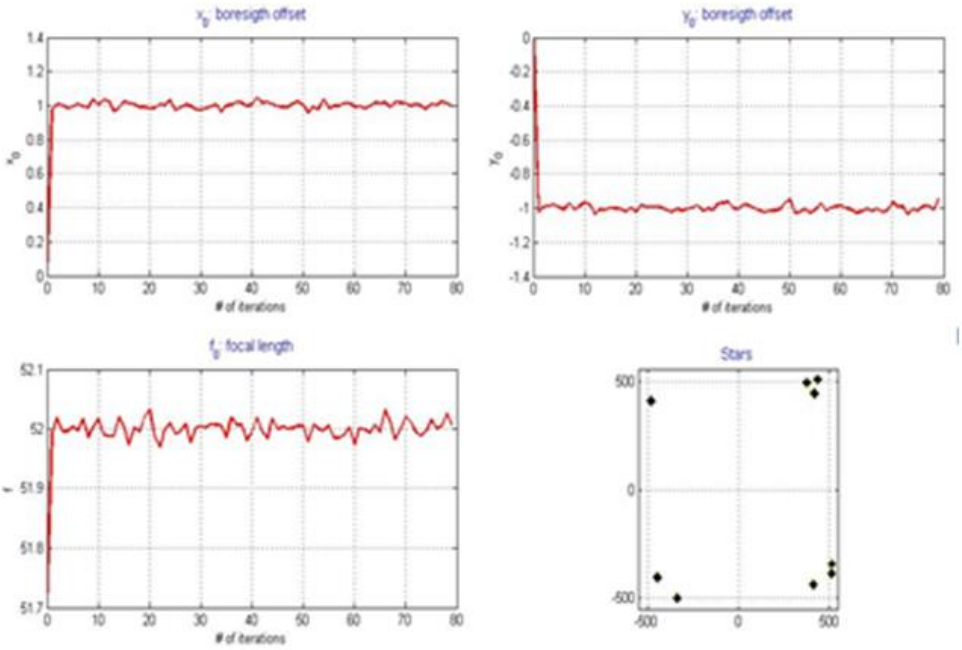

Fig. 25 – Filter results in a realistic noise perturbed case.

In order to assess the robustness of the algorithms, it has also to be considered the possibility of an erroneous identification of the imaged stars. This possibility has been investigated and the relevant findings are depicted in Fig. 26.

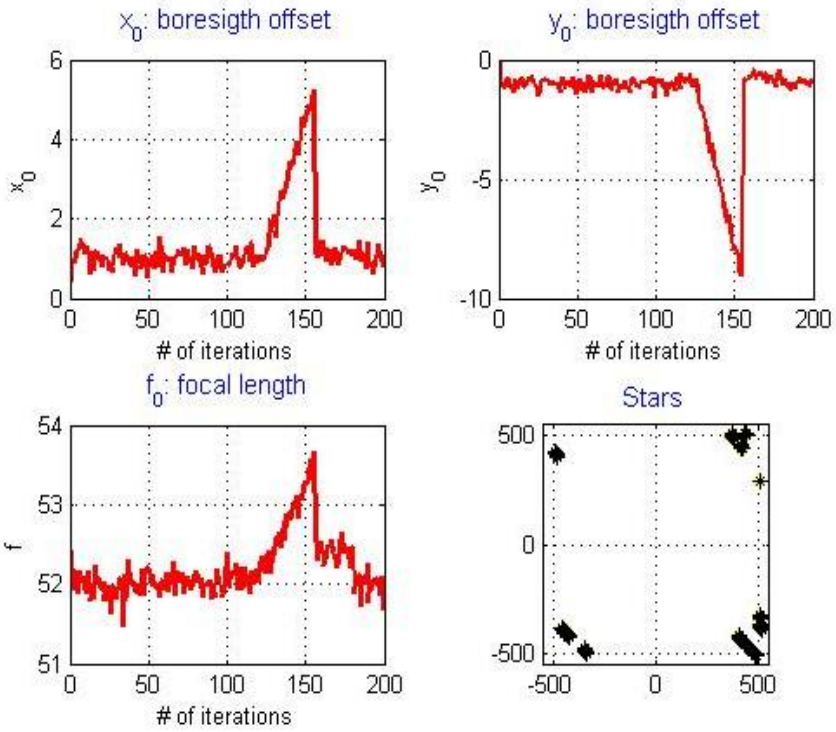

Fig. 26 – Results in case of some false star identification.

A clear divergence in the estimates of all the three unknowns appear at about the 120th iteration, to suddenly recovery the original value after 150th iteration. In order to explain this behaviour, Fig. 27 reports a zoom of the interval of interest.

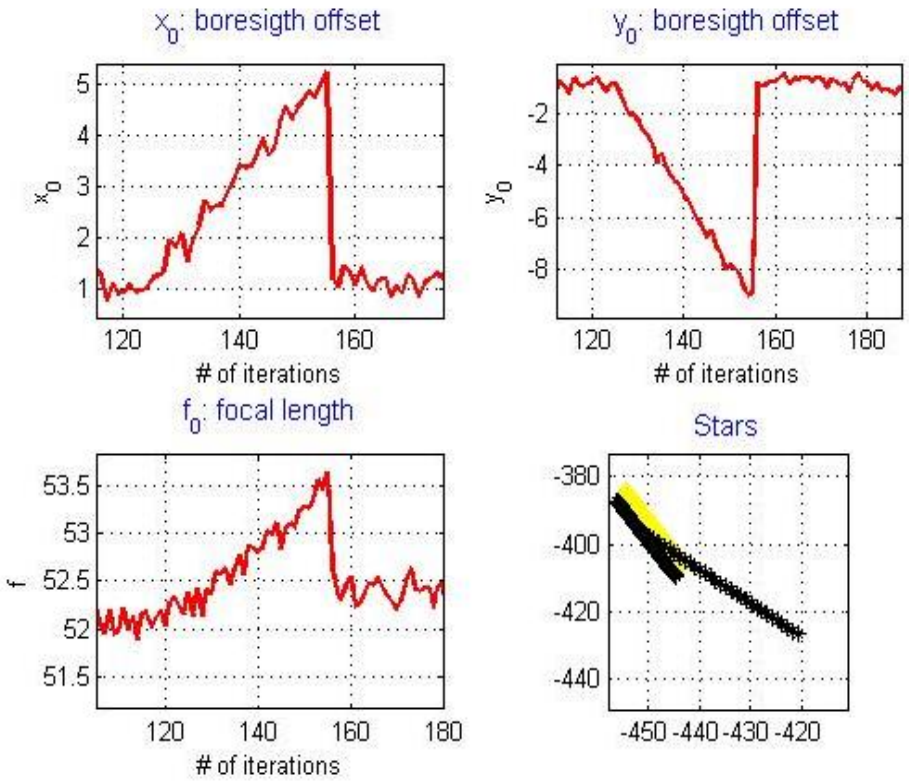

Fig. 27 – Detail of Fig. 26 case.

Looking at the image of stars captured by CCD, it is possible to appreciate that the catalogued stars (yellow line), differ from the measured stars (black line). Such a strong difference has been investigated, and it has been discovered that the difference depends on a false identification: indeed, black line and the yellow do not represent the same stars in this interval. As soon the correct identification comes back, the filter is able to promptly recover in a few iterations the right estimate, showing its robustness.

Conclusion

The trend in avionics to extend the use of star trackers to a wider class of spacecraft necessarily involves use of less expensive and simpler devices. A part of the cost reduction can be obtained by shortening long ground-based calibration campaign, and to directly estimate part of the important devices' parameters once in space. A possible two steps path (one at ground, the second in space) to tackle this issue has been presented in the paper. Specifically, results from the implementation of a Kalman filter to a realistic flow of images captured by the star tracker, together with their corresponding catalogue counterpart, are considered. The accurate evaluation of three parameters, namely the focal length and the coordinates of centre point, or better of their differences form ground-based estimates, follow.

3.5. High order contributors

3.5.1. Lens optical distortion effect

A high order contributor that affects the calibration parameters is the lens distortion. Distortion is an aberration arising not from a lack of sharpness of the image, but from a variation of a magnification with axial distance. If the magnification increases with increasing the axial distance, the outer parts of the fields are disproportionately magnified (see Fig. 28, Fig. 29).

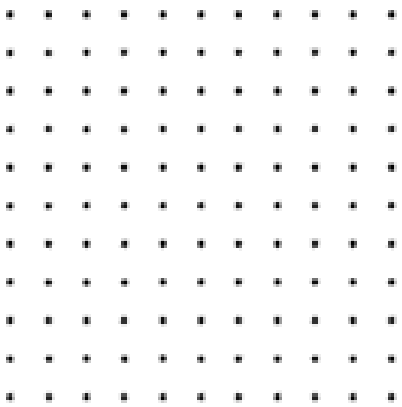

Fig. 28 – Square network NOT distorted

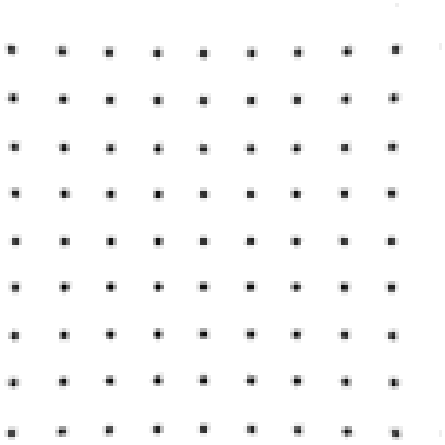

Fig. 29 – Pincushion distortion

This effect is called "*pincushion*" distortion. The opposite effect, when the magnification decreases with increasing axial distance, is called "*barrel*" distortion (see Fig. 30).

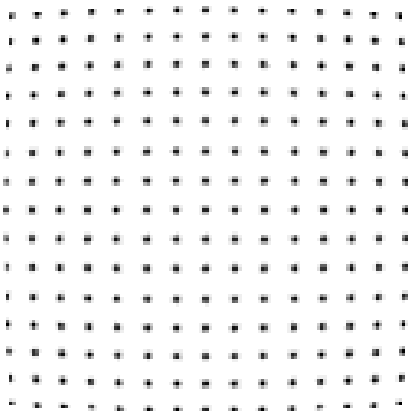

Fig. 30 – Barrel distortion

The effects of these aberrations are reported in the following figure (see Fig. 31).

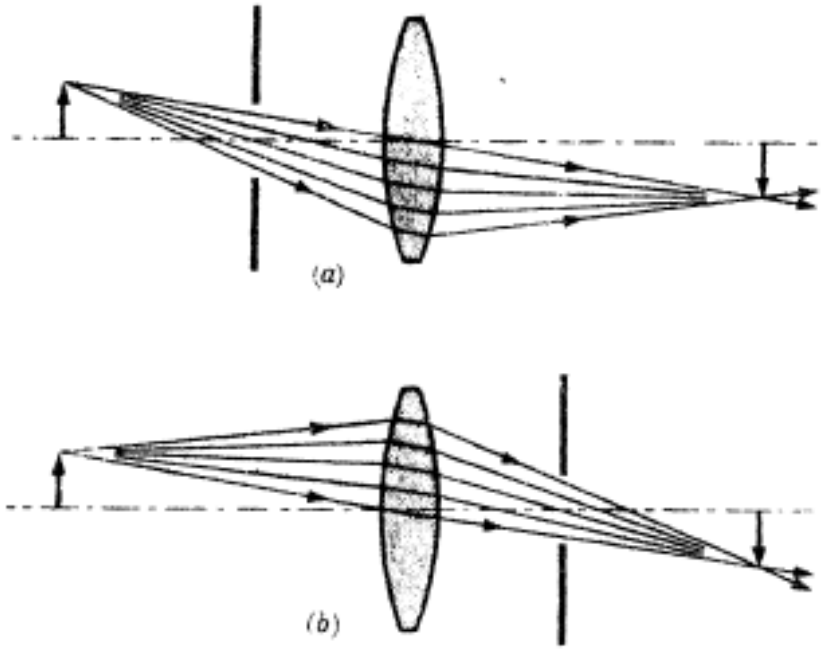

Fig. 31 – Effects of barrel (a) and pincushion (b) distortion.

Considering the projection of a unit vector $\hat{u}$ individuating a tracked star on CCD / APS plane:

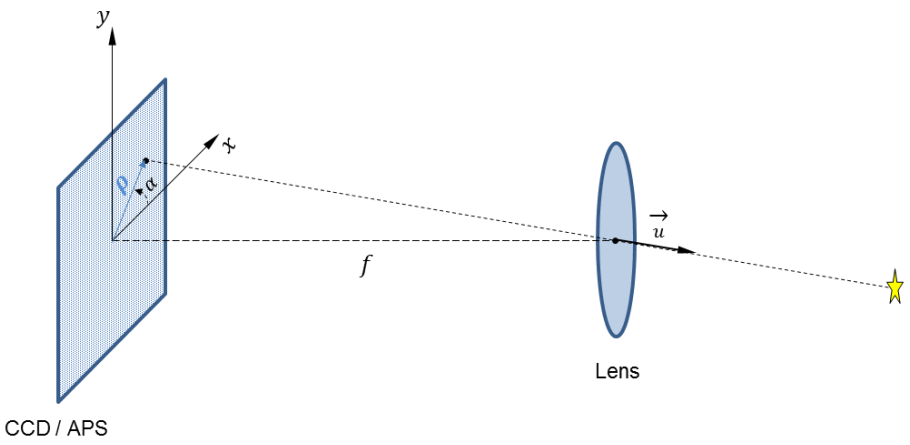

Fig. 32 – Projection of a star on CCD / APS plane

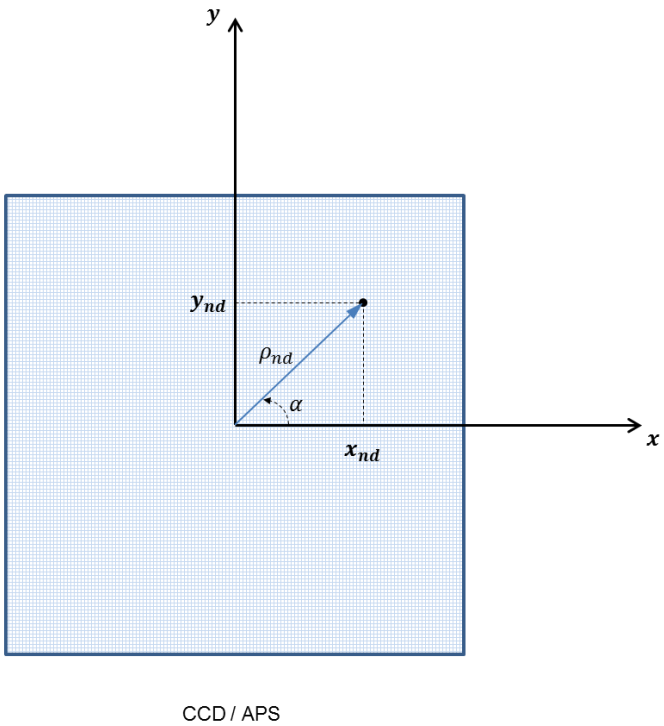

Fig. 33 – CCD / APS plane

The Cartesian components of the star (x, y) are:

$$\begin{cases} x_{nd} = k_0 + k_1 \cdot x_d + k_2 \cdot y_d + k_3 \cdot x_d \cdot (x_d^2 + y_d^2) + k_4 \cdot x_d \cdot (x_d^2 + y_d^2)^2 + k_5 \cdot x_d^2 + k_6 \cdot x_d \cdot y_d + k_7 \cdot y_d^2 \\ y_{nd} = h_0 + h_1 \cdot y_d + h_2 \cdot x_d + h_3 \cdot y_d \cdot (x_d^2 + y_d^2) + h_4 \cdot y_d \cdot (x_d^2 + y_d^2)^2 + h_5 \cdot y_d^2 + h_6 \cdot x_d \cdot y_d + h_7 \cdot h_d^2 \end{cases} \quad (4\text{-}20)$$

where:

- $\boldsymbol{x_{nd}}$ is the component along x-axis not affected by the distortion;
- $\boldsymbol{y_{nd}}$ is the component along y-axis not affected by the distortion;
- $\boldsymbol{x_d}$ is the component along x-axis affected by the distortion;
- $\boldsymbol{y_d}$ is the component along y-axis affected by the distortion;
- $\boldsymbol{k_i}$ $(\boldsymbol{i = 0, \dots, 7})$ are the calibration parameters for the component along x-axis;
- $\boldsymbol{h_i}$ $(\boldsymbol{i = 0, \dots, 7})$ are the calibration parameters for the component along y-axis.

In order to take into account also the lens optical distortion in the estimate of calibration parameters, the following model has been used:

- Radial optical distortion, described by the following equation [28]:

$$d = c_1\rho^3 + c_2\rho^5 + \cdots \qquad (4\text{-}21)$$

- Misalignments along x and y axes (rotation along bore-sight, i.e. z-axis)
- Offset

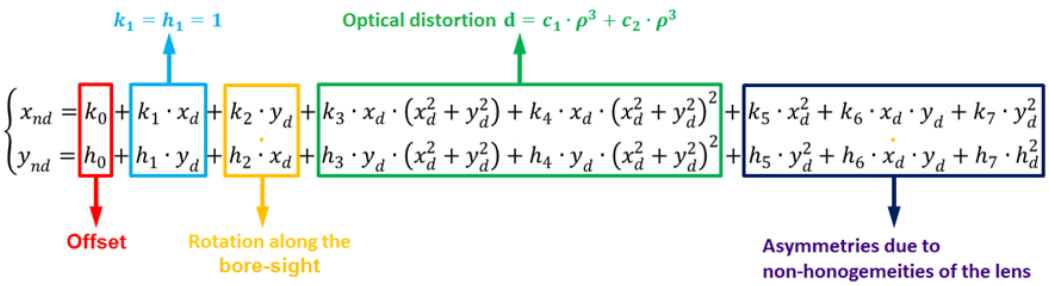

Fig. 34 – Equation modelling the not distorted components along x and y axes

3.5.2. Temperature effects on the focal length

The optics variation of temperature yields a variation on focal length. This behaviour is described by the following equation:

$$f_{T_{Optics}} = f_{nominal}\left[1 + \alpha_T\left(T_{Optics} - T_{nominal}\right)\right]$$

where:

- $f_{T_{Optics}}$ is the focal length at optics temperature T_{Optics} after its variation $T_{Optics} = T_{nominal} + \Delta T$;
- $f_{nominal}$ is the focal length at $T_{nominal}$.

Part III

Visual Navigation combining Star Tracker and Navigation Camera

4

Space Optical Navigation

4.1. Introduction

The exploration of the solar system is quickly advancing and more and more missions are bound to deep space, up to faraway planets, asteroids and comets.

Orbit determination of space probes and satellites is generally based on radio tracking from Earth and becomes clearly less accurate when the distance between Earth and S/C increases. Furthermore, also the time needed for telemetry uplink and telecommands downlink considerably increases distancing from Earth, making unattainable real-time manoeuvers and operations. As an example, the time needed to send a telecommand or receive telemetries in the Rosetta mission was about 20 minutes once the probe reached the target [29] [30].

When a more precise target-relative navigation is required, the optical navigation provide cross line-of-sight information to de-correlate estimates of spacecraft state from the target body ephemeris.

This technique was pioneered in the 1960s [31] and enabled successful navigation of the six Voyager flybys of the outer planets [32] and Cassini's orbital operations at Saturn [33]. Recently it was successfully used in the Rosetta [29] [30] and New Horizon [34] missions.

The increasing interest in this kind of missions has led to a lot of studies focused on the optical navigation improvement, both in the architecture and in the method. Cameras in the visible portion of the spectrum are routinely investigated and used in proximity operations, where they proved to be more accurate than any other technique [35] [36]. While they intrinsically provide angles-only information [37], they can be used together with an information about the size of the target to operate a complete 3D relative navigation manoeuvre [38].

The information about real size of the target can be known a priori or derived – as a distance measurement - from a sequence of observation from different point of view as in stereoscopic

imaging. These concepts can be exploited in different ways with different optical instruments: as an example, it has been explored the ability of earth-imaging sensors (part of the payload) to determine the orbital state using landmark tracking. Locations of these landmark in the images together with the information about payload camera pointing by gyros, star and sun sensors provide enough data to improve orbit determination [39]. An additional step could be the use, in some specific mission phase, of the same optical sensor to measure attitude and position. Due to the fact that star trackers are intrinsically really accurate, they are the best candidates for this universal sensor. Notice that the use of star tracker to capture celestial bodies' surface landmarks to improve orbital determination has been already proposed in [40]. A recent contribution [41] moves farther in investigating possible detailed technical solution in order to operate the star tracker with an obviously different light threshold, so to observe the surface instead of the stars in the black sky. Notice also that the twofold use of optical sensors for attitude and position determination has been explored in some experiment to overcome limitations of ground-based lab in reproducing space scenarios [42].

The aim of this study is to investigate and analyse the possible hardware configurations and software algorithms in order to use a star tracker as navigation camera. The availability of a universal

optical navigation sensor, sharing a large part of its expensive components, could really be an enabling technology for a more effective space exploration.

In the first part of the chapter will be presented a typical optical navigation system and the method used for the estimates of kinematics parameters. Then the discussion will be focused on the use of the star tracker as backup or in place of the navigation camera during the main phases of the mission: cruise, approach and fly-by or descend to the target. In the next part a simple case of study will be reported and its results will be presented and discussed.

4.2. Optical Navigation System

This section investigates a possible optical navigation system capable to provide – with a limited number of hardware components - both attitude and position determination.

4.2.1. Architecture

A complete optical navigation system should be composed by:

- **Star Tracker**, that estimates the attitude of the spacecraft w.r.t. the inertial reference frame;

- **LIDAR system**, intended as a distance measurement sensor, to returns very accurate ranging measurements w.r.t. the target. Notice that this LIDAR is intrinsically different from typical FLASH LIDARs, aimed instead to capture a 3D image of the full scenario.

  Navigation Camera, that obtains, through a sufficient wide field of view, the complete representation of the scenario and indeed helps in defining the relative position of the spacecraft with respect to the target.

4.2.2. Methods

Two types of optical navigation can be considered, namely star-based and landmark-based.

The star-based navigation is generally used during the cruise phase of the mission, in order to have a more accurate information of the target position. In this case the high accuracy is guaranteed by the knowledge of the stars in the background, accurate enough from catalogues.

The landmark-based navigation is generally related to the fly-by or descent to the targeted celestial body. In this case the estimate of the kinematics parameters by the landmark-based navigation can be done by:

- **absolute navigation**, that provides the absolute orbit information for the system, comparing the absolute measurements (recognized mapped landmarks, such as well-known craters and landforms, stored in an on-board catalogue) and measured landmarks (see Fig. 35).

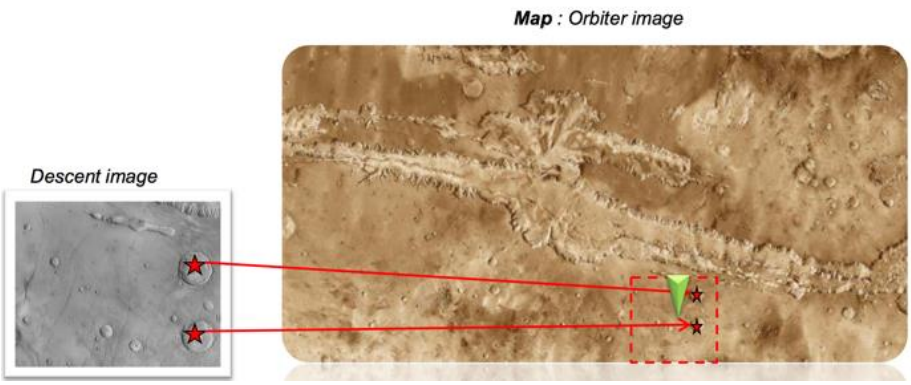

Fig. 35 – The comparison between « map » (images captured by the orbiter) and images captured during the descent leads to position / orientation estimation [43]

- **relative navigation**, that provides the relative position, attitude and velocity. In this case the landmarks coming from image features for which the location information is not known (such as cloud, shadows). The estimate can be computed by tracking these landmarks in consecutive images (see Fig. 36) and then fusing this information with on-board inertial measurements units (IMU) data [44].

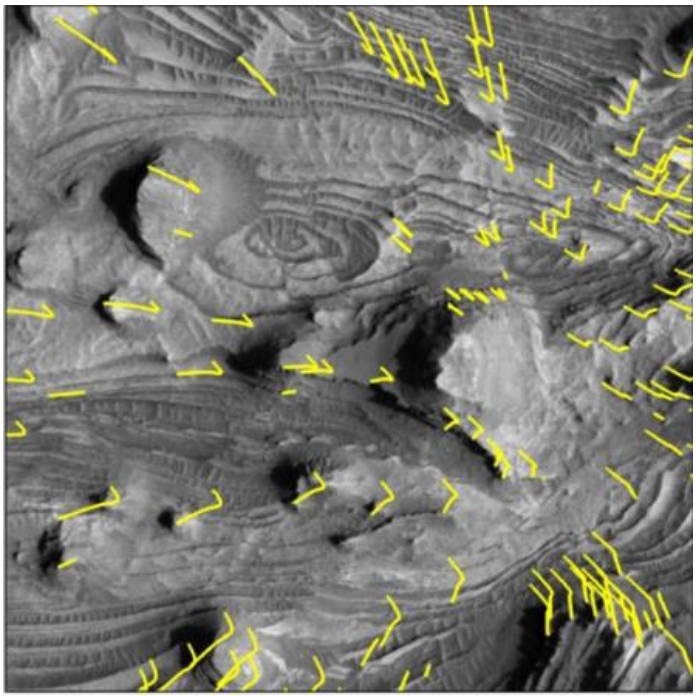

Fig. 36 – Relative landmarks tracked in consecutive images[43]

4.3. Star Tracker as Navigation Camera

The star tracker utilization as a universal optical navigation sensor or in redundancy of the navigation camera is generally not possible because the irradiance difference between the celestial body and the stars well-exposed is large. The problem can be solved by a robust algorithm or using a multi-head star tracker, i.e. a star tracker with different optics. This paragraph presents a brief description of how the start tracker can be used as navigation camera in the various phases of the mission.

4.3.1. Cruise and approach phases

During the cruise phase, at increasing of distance from Earth, the star tracker can evaluate a more accurate kinematics parameters of the target than the estimates coming from the radio tracking. A such approach has already studied for the OSIRIS-Rex and New Horizon mission, simulating a dedicated camera (see Fig. 37).

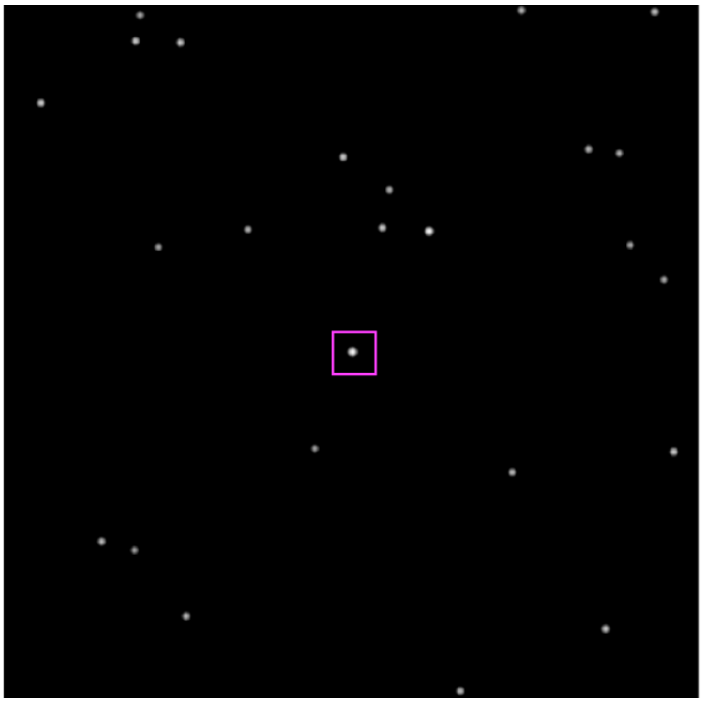

Fig. 37 – A simulated OSIRIS-REx PolyCam image of asteroid 1999 RQ36 on September 24th, 2018. The asteroid is in the centre of the magenta box, surrounded by field stars [47].

In order to study this method, a star tracker simulator has been prepared in a MatLab environment. An example is reported in the following figure (see Fig. 38).

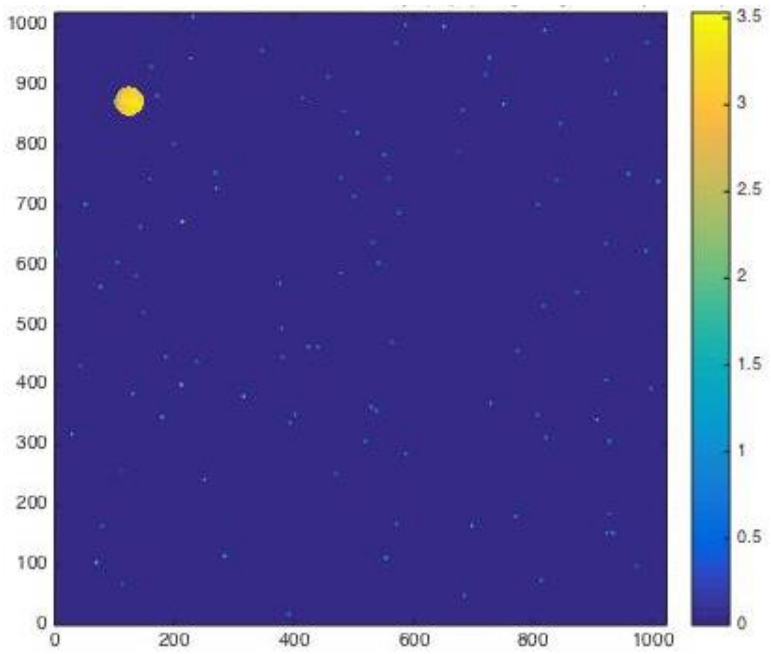

Fig. 38 – A simulated image of target surrounded by field stars.

In this phase the sensor manage the celestial body (target of the mission) as a Large Object, as shown in the figure. In this way, the star tracker is able to compute the position of the centroid of the target w.r.t. the optical centre of the image and the estimate of attitude and position and, then, we have all information to compute the best estimate of target kinematics.

4.3.2. Fly-by or landing phases

The use of star tracker as navigation camera changes when the space probe approaches the target and prepares the fly-by or landing phase. In this phase, in fact, the celestial body cannot be managed as a Large Object by the star tracker, because the target is too near to the sensor and blinds it. In this phase, the problem of insufficient dynamic range of the sensor has to be solved by software or by hardware, e.g. a multi-head star tracker with the two FOVs combined on the detector through a beam-slitter able to reduce the target brightness.

In that study, we consider the star tracker capable to enlarge its dynamic range. Therefore, the sensor can compute the estimate of the position w.r.t. the target according the method presented in the following flowchart (see Fig. 39):

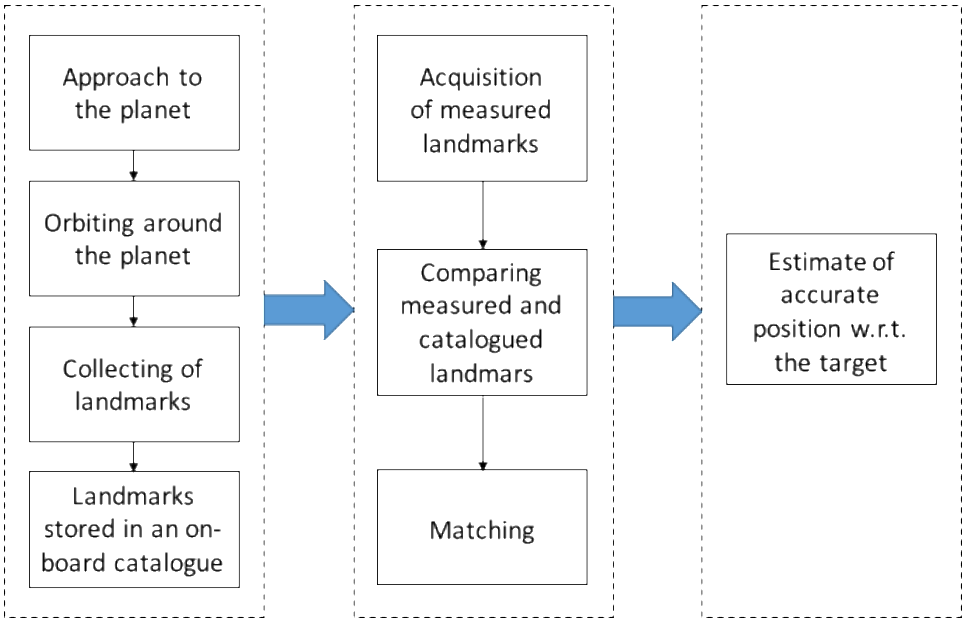

Fig. 39 – Flowchart of principal point to use the star tracker as navigation camera

The first phase of the method is focused on the collecting and storage of landmarks in an on-board catalogue (structured as the on-board star catalogue). For this reason the space probe will orbit around the celestial body till the landmarks catalogue is completed. During the second phase it will be exploited the functionality of star tracker to match the measured stars with catalogued stars (see section 2). In other words, the sensor uses the stored catalogued landmarks (collected during the first phase) to match the measured landmarks with the catalogued ones and to estimate the position w.r.t. the target.

In order to better explain the method, we consider the case in which the target is a planet and the landmarks are represented by craters (see Fig. 40), that are seen as circles (or ellipses) with their radius and orientation. The detection of the craters in the image can be easily tackled by algorithms based on Hough transform [49], that are especially effective in identifying simple geometric primitives.

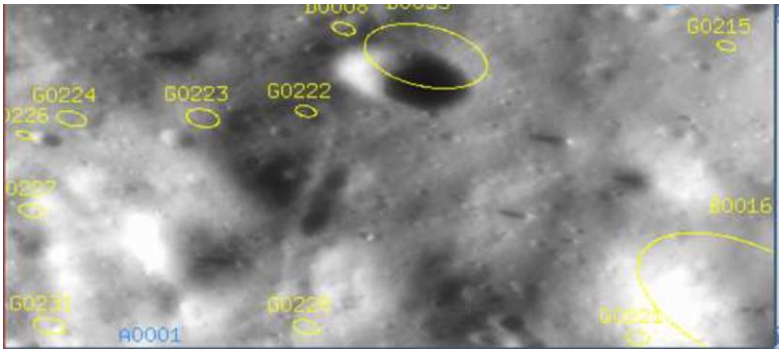

Fig. 40 – An example of land-marking of craters (NEAR mission) [48]

We identified the landmarks stored in the catalogue by:

- Identification number ID;
- Position (u_x, u_y, u_z) w.r.t. the Inertial Reference Frame located at centre of mass of planet and axes conveniently chosen;
- Radius of circle

As far as it concerns the differences between star catalogue and landmark catalogue, the first four parameters are similar (ID and

position w.r.t. a dedicated inertial reference frame), while the last is different as physical quantity, but similar in functionality. Indeed, it represents the star magnitude in the first case, and the radius of the circles in the second case.

Once the absolute landmarks are stored in an on-board catalogue, the star tracker works as for the stars and it is possible to evaluate the relative position w.r.t. the planet.

4.3.3. A case study

In the proposed case study, we consider a mission where the target is the moon and the landmarks have been stored on-board the spacecraft in a catalogue. An example on how the star tracker identifies and collect the landmarks is reported in the following figure (see Fig. 41).

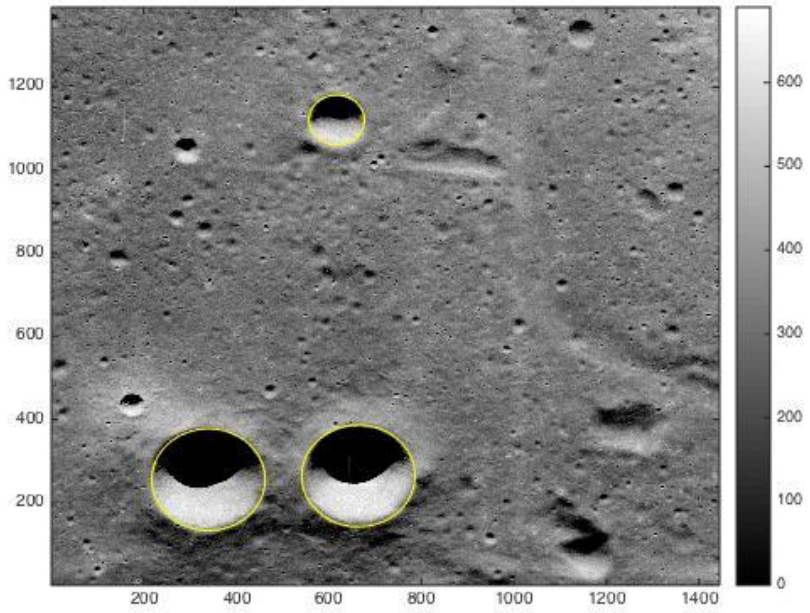

Fig. 41 – An example of land-marking of Moon craters by the sensor

The figure shows three craters on the Moon (marked by yellow circles) identified by the optical sensor. This craters will be stored in the catalogue following the scheme previously described: ID (landmark), position of the circle (u_x, u_y, u_z) and its radius.

The inertial reference frame $\mathrm{I} \equiv [\mathrm{I}_1, \mathrm{I}_2, \mathrm{I}_3]$ is located at centre of mass of the Moon. I3 axis is aligned with the Moon spin axis and the plane containing I1, I2 axes is parallel to the Moon equatorial plan. The spacecraft reference frame is coincident with the star tracker reference frame. For this simulation it is considered a multi-head star tracker, able to enlarge its dynamic range, the initial position known and the landmark already stored.

The optical head, used for the simulation, has been characterized as reported in the following:

- f = 152.5 mm
- FOV = 5° x 5°
- APS size = 1024 x 1024
- Pixel size = 13 μm

The results obtained by a MATLAB simulation are reported in the following figures (see Fig. 42):

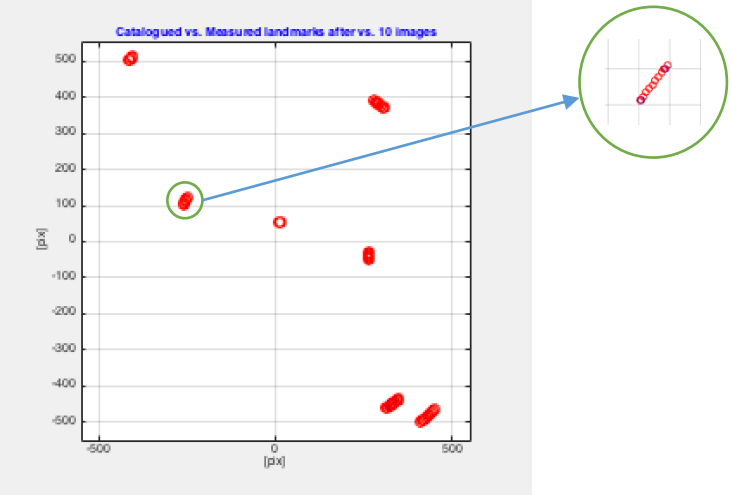

Fig. 42 – Results of the simulation measured (in red) vs. catalogued (in blue) landmarks.

The graph shows as the star tracker is able to estimate the position of the spacecraft, matching the measured landmarks (in red) with the catalogued ones (in blue). The estimate of the S/C position

(Right Ascension, Declination and Tilt) is reported in the following figures (see Fig. 43, Fig. 44, Fig. 45)

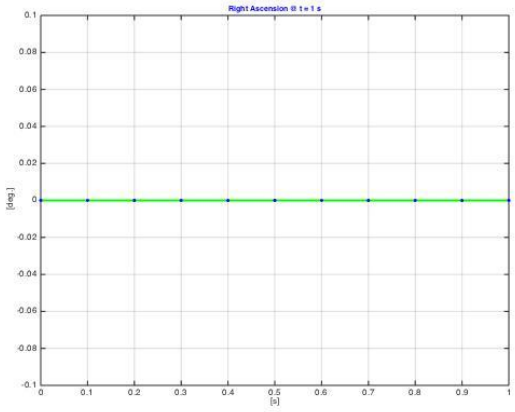

Fig. 43 – Estimate of S/C right ascension w.r.t. the inertial reference frame located at centre of mass of planet.

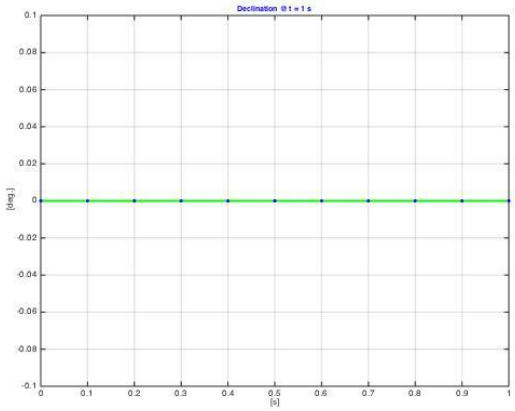

Fig. 44 – Estimate of S/C declination w.r.t. the inertial reference frame located at centre of mass of planet.

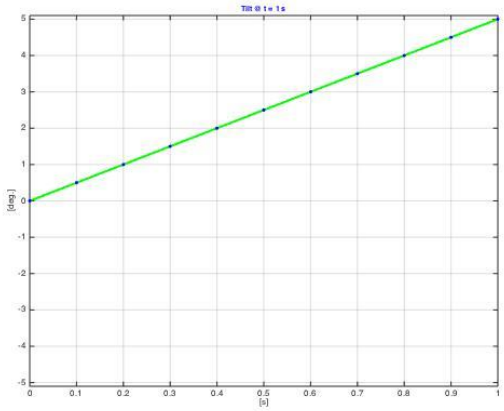

Fig. 45 – Estimate of S/C tilt w.r.t. the inertial reference frame located at centre of mass of planet.

The results are coherent with the simulation. Indeed, it has been performed for 1 second (with $sample\ rate = 100\ ms$) with initial position $(\alpha, \delta, TITL) = (0,0,0)$ and angular rate $\vec{\omega} = (0,0,0.5) rad/s$.

Conclusion

For this simple simulation, the star tracker has been able to compute the position of the spacecraft with respect to the planet inertial reference frame using the landmarks catalogue, as for the estimate of attitude.

The capability of a multi-head star tracker to estimate the relative position of the spacecraft with respect to a target, therefore acting as a navigation camera, opens the path to a universal optical sensor. The use of this sensor will be for sure limited to specific mission phases, due to the lenses' limitations and to the threshold

associated to the detector. As an example, the approach to deep space celestial bodies (asteroids, far planets) can be considered as a possible application regime. At least in these specific phases, the proposed solution has the potential to reduce the costs and/or offer a redundancy in case of failure of part of the instruments. Indeed, the analysis of this extended application of the star tracker is quite interesting for future deep space missions

Furthermore, the interest of the study is not limited to interplanetary navigation, and can be extended – by means of using multiple heads or specific filters - to other vehicles currently using star trackers and cameras as the planetary rovers.

References

[1] Wertz J. R. (ed.), *Attitude determination and Control*, Kluwer Academic Publishers, Dordrecht, (1978).

[2] Sabatini M., Palmerini G. B., Gasbarri P., "*Image-based control of the ''PINOCCHIO" experimental free flying platform*", Acta Astronautica, vol.94, pp.480-492 (2014).

[3] Liu H., Wang J., Tang J., Yang J., Jia H., *Autonomous on-orbit calibration of a star tracker camera*, Optical Engineering, vol.50, no.2 (2011).

[4] Shuster M. D., *Stellar Aberration and Parallax: A Tutorial*, The Journal of the Astronautical Sciences, Vo. 51, No. 4, pp.477-494 (2003).

[5] Sears F. W, *Optics*, Vol.3 of Addison-Wesley principles of physics series, University of California, (1945).

[6] Sidi M. J., *Spacecraft Dynamics and Control*, Cambridge University Press, U.S.A., (1997).

[7] Shepperd S. W., *Quaternion from rotation matrix*, AIAA Journal of Guidance and Control, Vol.1, No.3, pp.223-234 (1978).

[8] Shuster M. D., Oh S. D., *Three-Axis Attitude Determination for Vector Observations*, Journal of Guidance Control and Dynamics, Vol. 4, No.1, pp. 70-77 (1981).

[9] Markley F. L., *Attitude Determination using Vector Observations: A Fast Optimal Matrix Algorithm*, Journal of Guidance Control and Dynamics, Vol. 41, No.2, pp. 261-288 (1993).

[10] Wahba G., *A Least Squared Estimate of Satellite. Problem 65.1*, SIAM Review, pp. 385-386 (1966).

[11] Keat J., *Analysis of Least Squares Attitude Determination Routine. DOAOP*, Computer Sciences Corp., Report CSC/TM-77/6034 (1977).

[12] Enright J., Sinclair D., Fernando K. C., *COTS Detectors for Nanosatellites Star Trackers: A Case Study*, paper SSC11-X-1, 25th Annual AIAA/USU Conference on Small Satellites, Logan (USA), 2011.

[13] Shimmin R., Priscal C., Oyadomari K., Attai W., Wolfe J., Gazulla O. T., Salas A. G., *Using a smartphone camera for Nanosatellites attitude determination,* AMOSTECH – Advanced Maui Optical and Space Surveillance Technology Conference (2014).

[14] Khores A., Torres L., Nativel E., *Performance of a Smartphone base Star Tracker*, 4th Interplanetary Cubesat Workshop, London (2015).

[15] Sabatini M., Palmerini G. B., Gasbarri P., *Visual based Navigation of a Free Floating Robot by Means of a Lab Star Tracker*, Proceedings of the 12th International Conference on Informatics in Control, Automation and Robotics – ICINCO (2015) pp. 422-429.

[16] Gasbarri P., Sabatini M., Palmerini G. B., *Ground tests for vision based determination and control of formation flying spacecraft trajectories*, Acta Astronautica, 102 (2014) pp. 139-148.

[17] Sabatini M., Gasbarri P., Palmerini G. B., *Operational modal analysis via image technique of very flexible space structures*, Acta Astronautica, 89 (2013) pp. 139-148.

[18] Buemi M., Landi A., Procopio D., *Autonomous Star Tracker for Rosetta*, Proceedings of the 4th ESA International Conference on Spacecraft Guidance, Navigation and Control Systems (ESA SP-425), Noordwijk (The Netherlands), (1999) pp. 279-287.

[19] Enright J., Jovanovic I., Vaz B., *On-Orbit Star Tracker Recalibration: A Case Study*, IEEE Aerospace Conference Proceedings, (2015).

[20] Medaglia E., *Autonomous on-orbit calibration of a Star Tracker*, 3rd IEEE International Workshop on Metrology for Aerospace (MetroAeroSpace), Florence (Italy), (2016).

[21] Liu H. B., Wang J. Q., Tan J. C., Yang J. K., Jia H., *Autonomous on-orbit calibration of a star tracker camera*, Optical Engineering, vol. 50, no. 2 (2011).

[22] Samaan M. A., Griffith T., Singla P., Junkins J. L., *Autonomous on-orbit calibration of Star Trackers*, Core Technologies for Space Systems Conference (Communication and Navigation Session), (2001).

[23] Zarchan P., *Fundamentals of Kalman Filtering. A practical approach*, Vol. 246, Progress in Astronautics and Aeronautics, Fourth Edition, (2015).

[24] Reali F., G. B. Palmerini G. B., *Estimate problems for satellite clusters*, IEEE Aerospace Conference, Big Sky (USA), 2008.

[25] Sabatini M., Reali F., Palmerini G. B., *Autonomous State Estimation In Formation Flight*, IEEE Aerospace Conference, Big Sky (USA), 2007.

[26] Le X. H., Saburo M., *Fine-Tuning Kalman Filters Using Star Trackers Data for Micro Satellite Attitude Estimation*, SAIRAS, Turin (Italy), 2012.

[27] Liu H. B., Yang J. K., Wang J. Q., Tan J. C., Li X. J., *Star spot location estimation using Kalman filter for star tracker*, Applied Optics, 50:12 (2011) 1735-1744.

[28] Sears F. W., *Optics*, Addison-Wesley (1975).

[29] Hashimoto T., Ninomiya K., *Optical guidance for autonomous landing of spacecraft*, IEEE Transactions on Aerospace and Electronic Systems (Volume: 35, Issue: 2, Apr 1999).

[30] De Lafontaine J., *Autonomous spacecraft navigation and control for comet landing, Journal of Guidance, Control, and Dynamics*, Vol. 15, No. 3 (1992), pp. 567-576.

[31] Owen W. M. Jr., Duxbury T. C., Acton C. H. Jr., Synnott, S. P., Riedel J. E., and Bhaskaran S., *A Brief History of Optical Navigation at JPL.*, 31st Annual AAS Guidance and Control Conference. Breckenridge, CO, USA, 2008.

[32] Riedel J. E., Owen W. M. Jr., Stuve J. A., Synnott A. P., and Vaughan R. AM., *Optical Navigation During the Voyager Neptune Encounter*, AIAA/AAS Astrodynamics Conference, Portland, OR, USA, 1990.

[33] Gillam S. D., Owen W. M. Jr., Vaughan A. T., Wang T.-C. M., Costello J. D., Jacobson R. A., Bluhm D., Pojman J. L., and Ionasescu R., *Optical Navigation for the Cassini/Huygens Mission*, AIAA/AAS Astrodynamics Specialist Conference. Mackinac Island, MI, USA, 2007.

[34] Owen W. M., Jr., Dumont P. J., and Jackman C. D., *Optical Navigation preparations for New Horizons Pluto fly-by*, International Symposium on Space Flight Dynamics; 23rd; 29 Oct. - 2 Nov. 2012; Pasadena, CA; United States.

[35] Sabatini M., Palmerini G. B., Gasbarri P., *A Testbed for Visual Based Navigation and Control during Space Rendezvous Operations*. Acta Astronautica 117 (2015) 184–196.

[36] Masson A., Haskamp C., Ahrns I., Brochard R., Duteis P., Kanani K., Delage R., *Airbus DS Vision Based Navigation Solutions Tested on Liris Experiment Data*. ESA 7th Space Debris Conference 2017.

[37] Gaias G., D'Amico S., Ardaens J. S., "*Angles-Only Navigation to a Noncooperative Satellite Using Relative Orbital Elements*"; Journal of Guidance, Control and Dynamics, Vol. 37, No. 2, 439-451 (2014).

[38] Gasbarri P., Sabatini M., Palmerini G. B., *Ground tests for vision based determination and control of formation flying spacecraft trajectories*. ActaAstronautica 102 (2014) 378–391.

[39] Markley F. L., *Autonomous satellite navigation using landmarks*, in AAS/AIAA Astrodynamics Conference, North LakeTahoe, NV, 1981, pp. 989–1010.

[40] Zhang H., Kazemi L., Enright J., *Landmark-based Optical Navigation Using Nanosatellite Star Trackers*, Aerospace Conference, 2017 IEEE.

[41] Wang H., Jiang J., Zhang G., *Celestial Object Imaging Model and Parameter Optimization for an Optical Navigation Sensor Based on the Well Capacity Adjusting Scheme*. Sensors, Vol.17, No.4, (2017).

[42] Sabatini M., Palmerini G. B., Gasbarri P., *Visual based navigation of a free floating robot by means of a lab star tracker*, ICINCO 2015 - 12th International Conference on Informatics in Control, Automation and Robotics (2015).

[43] Bourdarias C., *Vision-based Navigation in Space*, Airbus Defence & Space 5th R&T Days, 20 Nov. 2014.

[44] Johnson A. E., Ansar A.,. Matthies L. H, Trawny N., Mourikis A. I., and Roumeliotis S. I., *A general approach to terrain relative navigation for planetary landing*, in AIAA Aerospace@ Infotech Conf., Rohnert Park, CA, 2007.

[45] Medaglia E., *Combined Ground-Based and In-Flight Calibration Processes for Star Trackers*, 67th International Astronautical Congress, Guadalajara, Mexico, 26-30 September 2016.

[46] Liu H. B., Wang J. Q., Tan J. C., Yang J. K., Jia H., "*Autonomous on-orbit calibration of a star tracker camera*", Optical Engineering, vol.50, no.2 (2011).

[47] Jackman C., Dumont P., *Optical navigation capabilities for deep space missions*, 23rd AAS/AIAA Space Flight Mechanics conference, Kauai, Hawaii, February 10 - 14, 2013.

[48] Owen W. M., Duxbury Jr. T. C., Acton C. H.,. Synnott Jr. S. P, Riedel J. E. and Bhaskaran S., *A brief history of optical navigation at JPL*, 31st annual AAS Rocky Mountain Guidance and Control Conference, 2008, pag. AAS 08-053.

[49] Casonato G., Palmerini G.B., *Visual techniques applied to the ATV/ISS rendez-vous monitoring*, IEEE Aerospace Conference Proceedings (2004).

[50] Saaman M. A., Mortari D., Junkins J. L., *Recursive Mode Star Identification Algorithms*, paper AAS 01-149 AAS / AIAA Space Flight Mechanics Meeting, Santa Barbara, California, Jan. 11 – Feb. 15, (2001).

[51] Ju G., Kim Y. H., Pollock T. C., Junkins J. L., Juang J. N., Mortari D., *Lost-In-Space: A Star Pattern Recognition and Attitude Estimation Approach for the Case of No a Priori Attitude Information*, paper of the 2000 AAD Guidance & Control Conference, Breckenridge, CO, Feb. 2-6, (2000).

[52] Junkins J. L., *Optimal Estimation of Dynamical Systems*, Sijthoff and Noordhoff International Publishers B. V., Alphan aan den Rijn, The Netherlands, (1978).

[53] Kowalick J., *Methods for Unconstrained Optimization Problem*, American Elsevier Publishing Company, New York, New York (1968).

[54] Crassidis J.L., Junkins J.L., *An introduction to Optimal Estimation of Dynamics Systems,* Chapman & Hall/CRC Applied Mathematics & Nonlinear Science, Second Edition, (2012).

[55] Crassidis J.L., Markley F.L., *State EstimationTechniques*, Book chapter in Spacecraft Orbit and Attitude System, edited by J.R. Wertz, (1978).

[56] Bertotti B., Farinella P., Vokrouhlikcky D., *Physics of the solar system. Dynamics and Evolution, Space Physics, and Spacetime Structure*, Kluwer Academic Publishers, Boston (USA), 2003.

[57] Kim S.G., Crassidis J.L., Cheng Y., Fosbury A.M., *Kalman Filtering for Relative Spacecraft Attitude and Position Estimation*, Journal of Guidance Control and Dynamics, Vol. 30, No.1, pp. 133-143 (2007).

[58] Cheng L., Zhaoying Z., Xu F., *Attitude Determination for MAVs Using a Kalman Filter,* Tsinghua Science and Technology, Vol. 13, No. 5, pp. 593-597 (2008).